Mertens and Kägi.[32] The validity of Eq. (13) is dependent on the assumption that the fluorescence originates from a point source.[33] The validity of this assumption, for the particular system under study, should be tested before application of this method by demonstrating that the dependence of the fluorescence of an appropriate standard on $[X_T]$ is indeed described by Eq. (13).

In conclusion, fluorescence analysis represents an easy way of studying protein–ligand interactions provided one can obtain an observable change in fluorescence due to ligand binding. The association constants describing the interaction can be obtained quite easily from conventional double reciprocal plots (Fig. 1) or plots of $1/(1 - \theta)$ vs $\theta/[X_T]$ (Fig. 2) for situations in which the concentration of bound ligand does not contribute appreciably to the total concentration of ligand. For this situation neither the plot of $1/(1 - \theta)$ vs $\theta/[X_T]$ nor the method of continuous variation[18,19] allows estimation of the stoichiometry of the interaction.

When bound ligand does contribute significantly to the total concentration of ligand both K_A and p can be obtained directly from a plot of $1/(1 - \theta)$ vs $\theta/[X_T]$. The method of continuous variation[18,19] can also be used to measure the stoichiometry. One should be aware of possible pitfalls in this analysis, such as nonlinearity of fluorescence change on fractional occupancy (Fig. 4) which can lead to gross errors in estimates of binding constants.[4] Possibly the greatest cause of error in these studies is failure to correct for inner filter effects. A variety of methods were presented which can correct for such trivial absorption of light, the method of choice being dictated by the conditions of study.

[23] Measurement of Metal–Ligand Distances by EXAFS

By ROBERT A. SCOTT

Introduction

Historical Preface

It has been only within the last decade that X-ray absorption spectroscopy (XAS) and the corollary technique of extended X-ray absorption fine structure (EXAFS) have become useful in examining biological systems. Although the phenomenon of X-ray absorption has been known since the

1920s,[1,2] a renaissance of interest occurred in the early 1970s when the Stanford Positron Electron Accelerating Ring (SPEAR) was first used as a source of synchrotron radiation. The unique characteristics (high intensity, brightness, broadband spectral distribution) of synchrotron radiation make it an ideal source for XAS and the Stanford Synchrotron Radiation Laboratory (SSRL) was established to make use of it. SPEAR was originally built to allow observation of subatomic particles created by collision of counterrotating bunches of positrons and electrons and thus, the first use of synchrotron radiation was "parasitic." SSRL currently receives 50% of SPEAR running for the "dedicated" production of synchrotron radiation. Other storage rings have also been used for synchrotron radiation research, but it is only recently (the last few years) that rings have been developed specifically for the production of synchrotron radiation.

The renaissance of XAS was also predicated on development of a theoretical basis for the EXAFS phenomenon, which came about during the early 1970s as well. The current theoretical understanding was sparked by the work of Sayers, Lytle, and Stern in 1970 on the single-scattering theory of EXAFS.[3-8]

Scope of This Chapter

It is the intended purpose of this chapter to discuss the methodology behind the use of EXAFS for determining metal–ligand environments (with specific application to metal sites in proteins and enzymes). This includes the collection, reduction, and analysis of X-ray absorption data. It does *not* include the theoretical basis of EXAFS. This will be covered only in outline, emphasizing those points required for an understanding of the methodology. In addition, no attempt has been made to survey the literature for applications of XAS to biological problems. Examples of such applications will be used only to illustrate the techniques discussed.

In addition, the edge and near-edge region of the X-ray absorption spectrum will be virtually ignored. This is not due to prejudice, since it is the author's opinion that studies involving the X-ray absorption edge

[1] W. Kossel, Z. *Phys.* **1,** 119 (1920).
[2] M. Siegbahn, "The Spectroscopy of X-Rays." Oxford Univ. Press, London and New York, 1925.
[3] D. E. Sayers, F. W. Lytle, and E. A. Stern, *Adv. X-Ray Anal.* **13,** 248 (1970).
[4] D. E. Sayers, F. W. Lytle, and E. A. Stern, *Phys. Rev. Lett.* **27,** 1204 (1971).
[5] D. E. Sayers, F. W. Lytle, and E. A. Stern, *J. Non-Cryst. Solids* **8–10,** 401 (1972).
[6] D. E. Sayers, F. W. Lytle, and E. A. Stern, *in* "Amorphous and Liquid Semiconductors," (J. Stuke and W. Brenig, eds.), p. 403. Taylor & Francis, London, 1974.
[7] E. A. Stern, *Phys. Rev. B: Solid State* [3] **10,** 3027 (1974).
[8] E. A. Stern, D. E. Sayers, and F. W. Lytle, *Phys. Rev. B: Solid State* [3] **11,** 4836 (1975).

(e.g., X-ray absorption near edge structure, XANES) will become increasingly important in providing electronic structural information. However, such techniques are still in their infancy compared to EXAFS and are much less amenable to discussion at this time.

Applicability of EXAFS

The XAS technique makes use of the fact that the energy dependence of the X-ray absorption coefficient (i.e., the X-ray absorption spectrum) of a material exhibits features characteristic of the elements contained in the material. For each element these features consist of a series of discontinuities (absorption edges) that occur at specific energies slightly affected by the electronic environment of the atom. In addition, if the atom is surrounded by a regular array of other atoms (e.g., in a crystalline matrix, or a homogeneous chemical compound), the absorption coefficient in the region of the spectrum just to higher energy of each absorption edge will exhibit oscillatory behavior, referred to as EXAFS. This spectral region contains structural information about the makeup of the "atomic neighborhood" of the absorbing atom. The EXAFS technique involves acquisition and analysis of data in the EXAFS spectral region in order to extract information concerning the local structural environment of the absorbing atom. Specifically, one can determine (1) the distance from the absorbing atom to other atoms; (2) the number of other atoms at a particular distance; and (3) the nature (i.e., atomic number, Z) of the other atoms.

The energy at which the X-ray absorption edge occurs is dependent upon the atomic number of the absorbing atom (see Fig. 1).[8a,8b] Thus, the range of elements available as absorbers in an EXAFS experiment is dictated by the availability of an adequate photon source in the appropriate energy region. For synchrotron radiation, the low-energy end of the range of available photon energies is affected by absorption of photons by window material, atmosphere, etc. With some special precautions (e.g., all He atmosphere), this places a lower limit of ~2.5 keV on available photons which makes the EXAFS experiment difficult for absorbing atoms with $Z \leq 17$ (Cl). There is no effective upper limit on the elements that can be examined as absorbers, since elements with K edges above the available photon energy range have L edges within the available range. As Fig. 1 shows, the available photon energy range must extend to ~25 keV to avoid gaps in the coverage of elements. This is usually not a problem

[8a] J. A. Bearden and A. F. Burr, *Rev. Mod. Phys.* **39**, 125 (1967).

[8b] W. H. McMaster, N. Kerr Del Grande, J. H. Mallett, and J. H. Hubbell, "Compilation of X-ray Cross Sections," UCRL-50174, Sect. II, Rev. 1. Natl. Tech. Inf. Serv., Springfield, Virginia, 1968.

with the current dedicated operation of synchrotron sources and the use of insertion devices such as wigglers.

For the most part, the transition metals are commonly used as absorbing atoms in EXAFS experiments on biological systems. Most typical is the use of EXAFS to examine the coordination environment of active sites in metalloproteins and metalloenzymes. Less typical but equally important are EXAFS studies of metal-binding sites (e.g., in calcium-binding proteins) and of appropriate atoms (e.g., As, Br, etc.) in inhibitors or substrates bound to (or near) metalloprotein active sites.

There are a few restrictions on the state of samples used in biological EXAFS studies. Physically, the sample may be a solution, frozen solution, lyophilized powder, microcrystalline solid, or single crystal. Chemically, one must take care to ensure as much homogeneity in the state of the metal site as possible. The EXAFS technique is notoriously poor at detecting heterogeneity in structural environments—only an average environment is found. A special case involves metalloenzymes with two or more atoms of the same metal in distinctive structural environments (e.g., cytochrome c oxidase, laccase, the iron sites in nitrogenase). In order to assign EXAFS features to individual sites, some kind of chemical perturbation must be used to alter the structure of one site while (presumably) not affecting the other(s). Generation of mixed valence states or "half-apo" protein is a possible approach to this problem.

Most recent EXAFS studies on biological systems have used the fluorescence excitation technique since its enhanced sensitivity makes it suitable for the lower concentrations accessible in biological samples. The sensitivity of the various fluorescence detection schemes dictates the lower concentration limit for EXAFS samples. This limit is dependent upon the atomic number of the absorbing atom and is currently $\sim$0.5–1.0 mM at Fe and $\sim$0.1–0.2 mM at Mo.

Theory

As already mentioned, it is not the purpose of this chapter to give a detailed discussion of the theory behind the use of the EXAFS technique for determination of metal environments. For those interested in the detailed mathematics, several treatments are available.[3–12] However, a certain amount of theory concerning the origin of EXAFS oscillations is

[9] C. A. Ashley and S. Doniach, *Phys. Rev. B: Solid State* [3] **11**, 1279 (1975).
[10] P. A. Lee and J. B. Pendry, *Phys. Rev. B: Solid State* [3] **11**, 2795 (1975).
[11] P. A. Lee and G. Beni, *Phys. Rev. B: Solid State* [3] **15**, 2862 (1977).
[12] P. A. Lee, *in* "EXAFS Spectroscopy. Techniques and Applications" (B.-K. Teo and D. C. Joy, eds.), p. 5. Plenum, New York, 1981.

necessary so that the reader can comprehend better the data analysis methodology.

X-Ray Absorption Spectrum

The shape of an X-ray absorption spectrum is controlled by the energies of dissociation of electrons from orbitals of the absorbing atom. There is a sharp discontinuity (an "edge") in the absorption spectrum in the region of these atomic ionizations. Dissociation of metal core ($n = 1$, 2) electrons usually requires photons in the X-ray range. Photodissociation of a 1s electron gives rise to the K-absorption edge while photodissociation of 2s or 2p electrons gives rise to the L edges. These events are
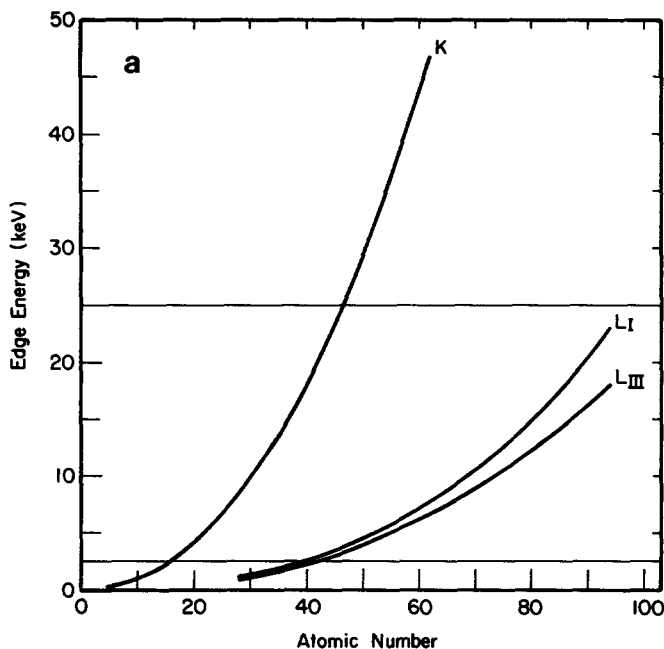

Fig. 1. X-Ray absorption edge energies. (a) The energy of the first inflection point of the elemental edge is plotted as a function of atomic number (Z) for K, L_I and L_{III} edges. A source giving off photons from ~2.5–25 keV allows coverage of all elements with $Z \geq 17$ (by either K or L_{III} edges). (b) Values of the energy of the first inflection point of the K and L edges for selected elements. The data are taken from the X-ray absorption energies tabulated by Bearden and Burr[8a] or from McMaster et al.[8b] In cases for which two values were available, the average was used. Values given in parentheses are those for which the two values disagreed considerably. In these cases, the values that fit better the trends in (a) were used.
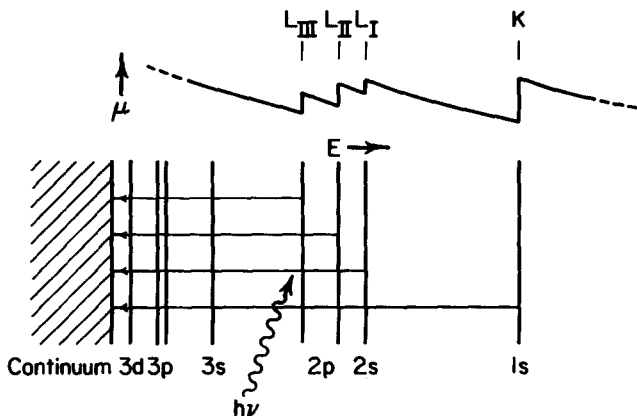
FIG. 1. (continued)

FIG. 2. General energy level diagram for X-ray absorption by an atom. The lower portion indicates the ionizations that give rise to the K, L_I, L_{II}, and L_{III} absorption edges indicated in the spectrum in the upper portion. The spectrum is plotted as absorption coefficient (μ) versus photon energy ($E \equiv h\nu$).

illustrated schematically in Fig. 2. Energies of K and L edges for selected elements are shown in the periodic table of Fig. 1.

We are interested specifically in the EXAFS region of the spectrum which starts ~50–100 eV beyond the absorption edge (see Fig. 3). In general, equivalent information is available from either K or L edge
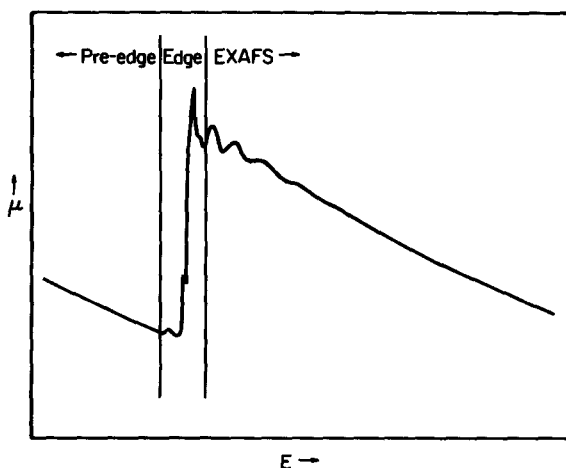
FIG. 3. General X-ray absorption spectrum indicating the energy regions of interest. Divisions between regions are poorly defined with the edge region entailing any features before, on, or just after the edge that are not analyzable as EXAFS.

EXAFS. L edge studies are generally done best using the L_{III} edge since the L_{II} EXAFS region is cut off early by the L_I edge and the L_I EXAFS region contains some remnant of L_{II} EXAFS. In any case, the EXAFS region contains oscillations on top of a smoothly varying background. Subtraction of this background (and normalization of the remainder by the size of the edge jump) yields the EXAFS data (the oscillations). It is this extraction of the EXAFS data and the subsequent analysis which are the subjects of this chapter.

Theoretical EXAFS Expression

A simple physical picture can be used to explain the oscillatory behavior of the EXAFS data. Upon absorption of an X-ray photon of energy E (where E is greater than E_0, the threshold energy for dissociation of the appropriate core electron), the atom is ionized, converting the bound electron into a photoelectron of wavelength λ. This wavelength is related to the photoelectron momentum, p, which is in turn related to the photoelectron kinetic energy [equal to $(E - E_0)$]. It proves convenient to define a photoelectron wave vector, $\mathbf{k}$, to use as the independent variable in displaying EXAFS data:

$$\mathbf{k} = 2\pi/\lambda = p/h = [2m_e(E - E_0)/\hbar^2]^{1/2} = [0.262449 \, (E - E_0)]^{1/2} \quad (1)$$

The final expression holds for E and E_0 expressed in units of electron volts (eV) and $\mathbf{k}$ in units of Å^{-1}.

Since no EXAFS is observed in the X-ray absorption spectrum of a monoatomic gas (e.g., Kr), it was postulated that the EXAFS oscillations arose from backscattering of this X-ray-induced photoelectron from the nuclear potentials of nearby atoms. Using this picture, the absorption coefficient would be proportional to the amplitude of the backscattered photoelectron wave at the absorbing atom. Since this amplitude is periodic (i.e., we can treat the photoelectron as a wave) and λ is inversely proportional to the square root of the kinetic energy $(E - E_0)$, the absorption coefficient would be expected to have an energy dependence proportional to the interference between the outgoing and backscattered photoelectron waves. Figure 4 gives a schematic illustration of this argument. At photon energy E_1 (Fig. 4a), the backscattered wave "arrives back" at the absorbing atom in phase giving constructive interference and a maximum in the absorption coefficient (Fig. 4c), whereas at photon energy E_2 (Fig. 4b), the interference is destructive giving a minimum in the absorption coefficient.

Thus, each scattering atom is expected to give rise to a periodic oscillation of the absorption coefficient and the EXAFS turns out to be a sum
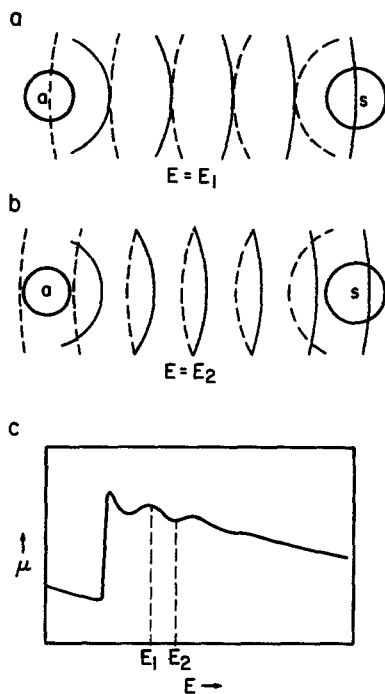
FIG. 4. Diagrammatic representation of the scattering processes that give rise to the EXAFS. (a) The outgoing and backscattered waves at energy E_1 giving rise to constructive interference and a maximum in μ. (b) The scattered waves at energy E_2 giving rise to destructive interference and a minimum in μ. [In both (a) and (b), the solid arcs represent the "peaks" of the outgoing wave from absorber a and the dashed arcs represent the "peaks" of the backscattered wave from scatterer s.] (c) The resulting spectrum indicating the values of μ at E_1 and E_2.

of damped, phase-shifted sine waves, one from each (set of) scatterer(s). This can be expressed mathematically in terms of the EXAFS (χ) as a function of the photoelectron wave vector (**k**):

$$\chi(\mathbf{k})\left(\equiv \frac{\mu - \mu_s}{\mu_0}\right) = \sum_s \frac{B_s N_s |f_s(\pi, \mathbf{k})|}{\mathbf{k} R_{as}^2}$$

$$\exp(-2\sigma_{as}^2 \mathbf{k}^2)\ \sin[2\mathbf{k}R_{as} + \alpha_{as}(\mathbf{k})] \quad (2)$$

The first equivalence describes the empirical extraction of $\chi(\mathbf{k})$ from the total absorption coefficient (μ) by subtraction of the smooth background (μ_s) and normalization to the free-atom absorption coefficient of the same edge height (μ_0). The theoretical expression was derived assuming single-

scattering theory, but contains the extra factor, B_s. The summation over s is to be interpreted as a summation over all scatterers, s, or over all shells of scatterers, s. In this context, a "shell" of scatterers means a collection of scatterers (all of the same element) at (approximately) the same distance from the absorber. N_s is the number of scatterers in such a shell and R_{as} is the distance (or weighted average of the distances) of the scatterers in this shell from the absorber, a.

The exponential term is referred to as the Debye–Waller factor and it describes the damping (in k-space) of χ due to the relative mean square deviation (σ_{as}^2) in R_{as}. Actually, σ_{as}^2 results from the combination of two effects:

$$\sigma_{as}^2 = \sigma_{vib}^2 + \sigma_{stat}^2 \tag{3}$$

σ_{vib}^2 represents the dynamic contribution due to vibrational motion of atoms a and s. This may be calculated assuming a harmonic vibration of frequency ν.[13]

$$\sigma_{vib}^2 = (h/8\pi^2\mu\nu)\coth(h\nu/2kT) \tag{4}$$

μ is the reduced mass of the a–s system, T is the absolute temperature, and h, k are Planck's and Boltzmann's constants, respectively. σ_{stat}^2 represents the contribution from static disorder in the interatomic distances that make up the shell. This can be estimated for a shell containing m atoms at distance R_m and n atoms at distance R_n.[13,14]

$$\sigma_{stat} \approx \frac{(mn)^{1/2}}{(m+n)}|R_m - R_n| \tag{5}$$

This usually holds only for moderately disordered systems ($|R_m - R_n| \lesssim 0.1$ Å).

The overall appearance of the EXAFS contribution from a shell is dependent upon the nature of the absorbing atom and (particularly) the scattering atom(s). In this dependence lies the main utility of the technique (i.e., the identification of the type of scattering atom from the shape of the EXAFS). This dependence is described by an inherent backscattering function which is broken up into amplitude and phase components in Eq. (2). The inherent backscattering amplitude is denoted as $B_s|f_s(\pi,k)|$. This amplitude is a function of k and is often referred to as the amplitude envelope. The phase component is denoted $\alpha_{as}(k)$, the inherent backscattering phase shift, which is also a function of k.

[13] B.-K. Teo, *Acc. Chem. Res.* **13**, 412 (1980).
[14] B.-K. Teo, R. G. Shulman, G. S. Brown, and A. E. Meixner, *J. Am. Chem. Soc.* **101**, 5624 (1979).

B_s is a factor which is best described as the product of two other factors:

$$B_s = S_s T_s \tag{6}$$

S_s is a scale factor and T_s is a transmission factor. S_s is needed to correct errors in theoretically derived amplitude envelopes. T_s is usually assumed to be unity for "first shell" scatterers, but may be less than unity for longer distance scatterers. It may be used to correct for multiple scattering effects or for inelastic scattering losses of photoelectron amplitude. The latter effect is sometimes described by a factor of the form, $\exp(-R_{as}/\lambda)$, where λ is a mean free path for the photoelectron.

The types of information that are available from an EXAFS spectrum should be clear from the discussion so far. In each component "sine" wave there are basically three observables: frequency, amplitude, and phase. Measurement of the frequency ($\sim 2kR_{as}$) gives information about the absorber–scatterer distance, R_{as}. Measurement of the amplitude gives information about the number of scatterers, N_s, in the shell. Measurement of the phase [α_{as} (k)] gives information about the type of atom doing the scattering. As already discussed, there is also information concerning the type of scatterer in the shape of the amplitude envelope [$B_s | f_s(\pi, k)|$]. In all of the above, the treatment has been oversimplified. A more detailed description must be delayed until the discussion of data analysis.

Experimental Techniques

One trigger event for the renaissance of XAS as a powerful structural technique was the advent of synchrotron radiation as an X-ray source for these experiments. Certainly, application of EXAFS to biological systems would not be possible without synchrotron radiation sources. In this section, the discussion will involve the components of a typical "X-ray absorption spectrometer" and the methodology of data acquisition and data analysis. Of particular interest are discussions of potential experimental difficulties and the inherent limitations of the EXAFS technique.

X-Ray Absorption Spectrometer

Figure 5 illustrates diagrammatically the general equipment components necessary to perform XAS measurements. These include a source of X rays, some means of energy resolving this radiation (one type of monochromator is shown, but dispersive elements may be used alternatively), and detection equipment. In addition, a means of control of spectrometer operation and data acquisition is required. In the case of XAS, a (dedicated) computer plays this role.
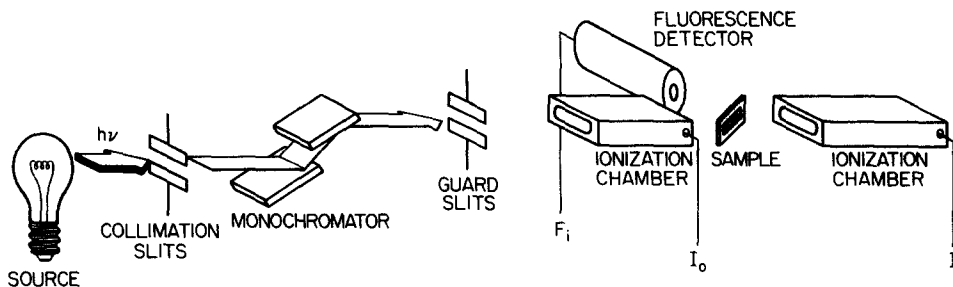
FIG. 5. The components of a general X-ray absorption spectrometer. The X-ray source is typically synchrotron radiation (not a light bulb). The monochromator shown is that described in Fig. 6b. The detection system can measure either transmission [$\mu x = \ln (I_0/I)$] or fluorescence excitation ($\mu x \propto \Sigma_i F_i/I_0$) spectra.

Source. For biological applications, the source requirement is for X-ray photons between ~2.5 and 25 keV. Other necessary features are a fairly flat spectrum (white radiation), high intensity (because of inherently dilute samples), and high collimation (so that small sample volumes can be used). The energy range requirement is fulfilled by three types of sources: conventional sealed-tube X-ray sources, rotating anodes, and synchrotron radiation.

Conventional X-ray tubes (e.g., a copper target source) produce a spectral distribution consisting of a Bremsstrahlung background with characteristic emission lines (e.g., copper K_α, K_β emissions). In order to scan the X-ray photon energy, the Bremsstrahlung background must be used and typical photon fluxes (through a 0.1-mrad² aperture, for example) are ~10^4 photons sec^{-1} eV^{-1} at 10 keV. In rotating anode X-ray tubes, the target is rotated (to increase the effective target surface area), allowing higher photon fluxes to be obtained (ca. one to two orders of magnitude higher than a similar conventional X-ray tube). The source spectrum still contains features characteristic of the target material. Thus, these sources give distinctly "nonflat" spectral distributions. This can be overcome partially by choosing the target material wisely. Their main disadvantage is their low photon flux, which has so far precluded their use with dilute metalloprotein samples.

SSRL was the first storage ring used as a synchrotron radiation source, but since then many more storage rings and synchrotrons have become available for XAS work. In the United States there are three main synchrotron radiation sources available for biological XAS: SSRL, the Cornell High Energy Synchrotron Source (CHESS) at Ithaca, New York, and the National Synchrotron Light Source (NSLS) at Brookhaven, Upton, Long Island. (As of this writing, the NSLS was still not fully commis-

sioned.) In general, synchrotron radiation has the advantage of being fairly "white" (flat spectral distribution). It also displays extremely high brightness resulting from high intensity and high collimation. For a 0.1-mrad^2 aperture, fluxes can be easily $\gtrsim 10^{10}$–10^{11} photons sec^{-1} eV^{-1} at 10 keV. With incorporation of insertion devices (e.g., wigglers), these fluxes can be increased by as much as two to three orders of magnitude. It is clear from this discussion that synchrotron radiation is the "source of choice" for biological XAS work.

Distribution of synchrotron radiation beamtime to the user community is done for the most part by proposal. A prospective user submits a proposal to perform specific experiments, requesting a certain amount of beamtime. A system of external peer review is used to evaluate the scientific impact of the work and the competence of the investigator(s). Based on the reviews, a rating is assigned (at SSRL by a Proposal Review Panel) to each proposal and this rating is used to decide on scheduling of beamtime. At SSRL in 1983, about 60% of the proposals that were rated and requested beamtime actually received beamtime.

At the NSLS (and also at SSRL), a different mode of operation is also being used. This involves the establishment of a Participating Research Team (PRT), usually made up of both academic and industrial concerns. The PRT is usually requested to make both a scientific and financial commitment to setting up an experimental station at the facility, in return for which they are guaranteed a certain percentage of the beamtime available on that station. In all cases to date, some fraction of the time is also set aside for peer-reviewed proposals. The most recent example of the PRT approach is the construction of beam line VI at SSRL jointly by Exxon, Lawrence Berkeley Laboratory (LBL), and SSRL. This beam line was commissioned in spring, 1984.

Monochromator. In recording XAS data, the normal procedure involves collecting data points at discrete photon energies, one at a time. This procedure requires monochromatization of the white source radiation. In general, this is accomplished by taking advantage of Bragg reflection from a certain diffraction plane of a single crystal:

$$n\lambda = n\left(\frac{hc}{E}\right) = 2d \sin \theta \tag{7}$$

where n is the order of the reflection, λ is the wavelength of the diffracted ray, E is the energy of the diffracted ray, d is the d-spacing of the crystal lattice planes, θ is the angle between the Bragg planes and the incident ray, h is Planck's constant, and c is the speed of light. For energies in the proper region (2.5 keV $\leq E \leq$ 25 keV) and reasonable incident angles (θ), the optimum d-spacing is ~1.5–3.5 Å (for use of a first order reflection, $n = 1$). Typical crystal planes used for X-ray monochromators include

Si[111], Si[220], Si[400], Ge[111], Ge[220], Ge[311], etc. Silicon proves to be a good choice since large single crystal specimens of silicon are available for cutting and polishing.

Flat crystal monochromators make use of crystals polished parallel (or nearly parallel) to a set of Bragg planes. Several different arrangements have been tried (at one time or another). These are illustrated in Fig. 6a–d. The simplest arrangement involves a single flat crystal rotated during the scan to different incident angles (θ). This arrangement is clumsy since the experiment (sample and detectors) has to track the reflected beam during the scan. Figure 6b shows a conventional double crystal monochromator (as used at SSRL, for example) in which the incident beam is Bragg reflected from two flat crystals in succession resulting in a reflected ray parallel to the incident ray. The crystals are mounted on a goniometer at fixed separation and the goniometer is rotated by computer-controlled stepping motors to effect a scan. As a result of the fixed intercrystal separation, the vertical position of the beam changes during the scan. This is usually compensated by moving a stepping motor-controlled table (with the experiment) vertically to track the reflected beam. The advantage of using this monochromator lies in its ease of construction and operation.

There are two possible arrangements that can avoid movement of the reflected beam during a scan (at the expense of extra complexity in the mechanisms). The double–double crystal monochromator is shown in Fig. 6c. In this case, two pairs of fixed-separation crystals are rotated in tandem in opposite directions. Figure 6d shows the variable-separation double crystal monochromator (the Golovchenko design). During a scan, both crystals are rotated and kept parallel to each other while one is also moved horizontally (on an air bearing) so that the reflected ray is always at the same vertical position. The last two monochromators are both "fixed-in, fixed-out" monochromators. For any of the monochromators that need two (or more) crystals with parallel Bragg planes, some sort of tuning mechanism is required to assure alignment. In the current double crystal design at SSRL, a piezoelectric stepper on one crystal is used for tuning.

Figure 6e illustrates a bent-crystal focusing monochromator of a design often used with laboratory sources (e.g., rotating anodes) to enhance the photon intensity collected from the source.[15-18] Increases of as much as three orders of magnitude in photon flux have been reported.[15] In a

[15] G. S. Knapp, H. Chen, and T. E. Klippert, *Rev. Sci. Instrum.* **49**, 1658 (1978).

[16] G. G. Cohen, D. A. Fischer, J. Colbert, and N. J. Shevchik, *Rev. Sci. Instrum.* **51**, 273 (1980).

[17] R. Haensel, *AIP Conf. Proc.* **64**, 73 (1980).

[18] S. Khalid, R. Emrich, R. Dujari, J. Shultz, and J. R. Katzer, *Rev. Sci. Instrum.* **53**, 22 (1982).
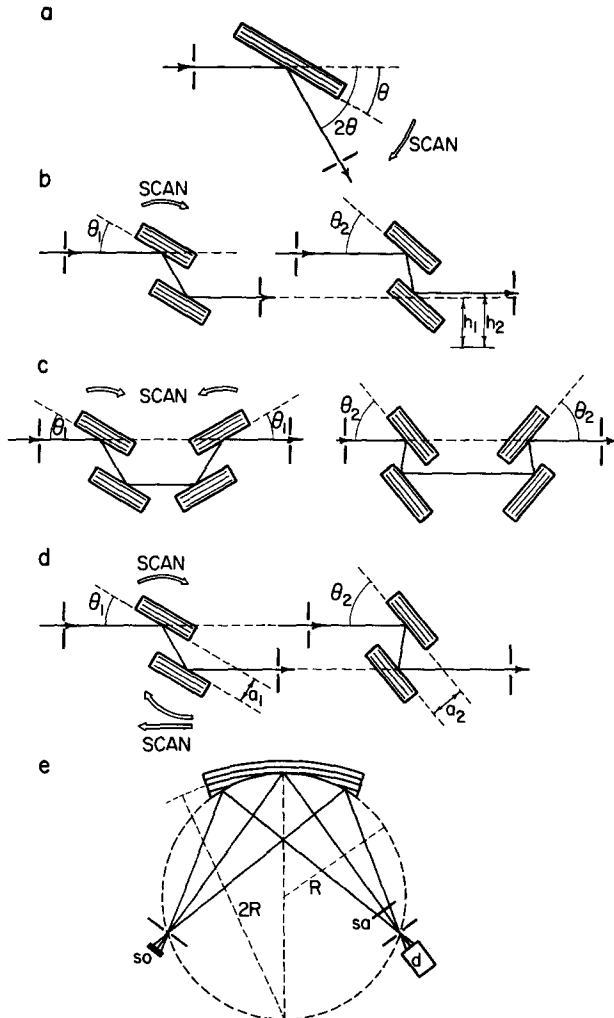
FIG. 6. Various designs for crystal X-ray monochromators that make use of Bragg reflection. Each diagram illustrates the diffracting crystal(s) in cross section (the lines indicate the Bragg planes) and typical ray-tracings. (a) A simple flat crystal monochromator. (b) The common double crystal (fixed separation) monochromator. (c) A double–double crystal (fixed separation, fixed in/fixed out) monochromator. (d) The Golovchenko double crystal (variable separation, fixed in/fixed out) monochromator. (e) A bent crystal monochromator using the Johansson geometry (d, detector; sa, sample; so, source). This latter type of monochromator is typically used with a laboratory X-ray source.

scan, as the bent crystal is rotated by θ, the sample and detector are rotated about the same pivot by 2θ.

It is of interest to mention here the importance of resolution (spectral bandwidth) of the various monochromators already discussed. For EX-AFS data, a spectral bandwidth of 10–20 eV is sufficient since EXAFS oscillations occur over $\gtrsim 50$ eV. However, if one is interested in X-ray absorption edge structure as well, ~ 2 eV resolution is required. There is *always* a trade-off between resolution and intensity. For flat crystal monochromators, the resolution is given by

$$\Delta E = E(\Delta \theta) \cot \theta \tag{8}$$

convolved with the rocking curve of the crystal reflection being used. In Eq. (8), θ is the Bragg angle at photon energy E and $\Delta \theta$ is the spread in θ for rays passing through the monochromator. For synchrotron radiation, $\Delta \theta$ is defined by the vertical collimation of the radiation entering the monochromator (see Fig. 5). For a typical high-resolution XAS scan at SSRL, the vertical aperture might be ~ 1 mm at 20 m from a 1-mm-high source point. This gives $\Delta \theta \approx 0.1$ mrad and for a Bragg reflection with a sufficiently narrow rocking curve (e.g., Si[220]), $\theta = 18.84°$ at 10 keV and Eq. (8) gives $\Delta E \lesssim 3$ eV ($\Delta E \lesssim 2$ eV at 8 keV). If the vertical aperture is opened to 2 mm, a 2-fold increase in photon flux is available in exchange for a 2-fold decrease in resolution. A typical bent-crystal focusing monochromator might give resolution of ~ 10–15 eV[15] due to the broad rocking curve of the bent crystal and the nonideal source image (i.e., it is not a line source). This can be improved somewhat (again accompanied by lower photon flux) by inserting a "flag" pointed toward the center of the bent crystal (the flag would be moved up in Fig. 6e). This allows only a smaller cone of rays to be incident on and reflected from the crystal.

In some experiments utilizing synchrotron radiation, the beam is first reflected off a focusing mirror before passing through the monochromator. These mirrors are generally bent toroidal mirrors (Pt-coated fused quartz, for example) which are designed to collect a larger portion of the beam and focus it into a spot at the sample, increasing the brightness by a significant factor. It should be realized that such focusing mirrors degrade the resolution of the photon energy substantially. Figure 7 shows that this is a result of the mirror converting the horizontal divergence of the beam into vertical convergence which then contributes to $\Delta \theta$ in Eq. (8). Often, horizontal collimation of the beam (*before* the mirror) by the use of a vertically positioned "V"-slit is used to improve resolution (again, at the expense of photon flux).

X-Ray Detectors. The absorption coefficient, μ, of a sample of thickness x can be measured using the relationship
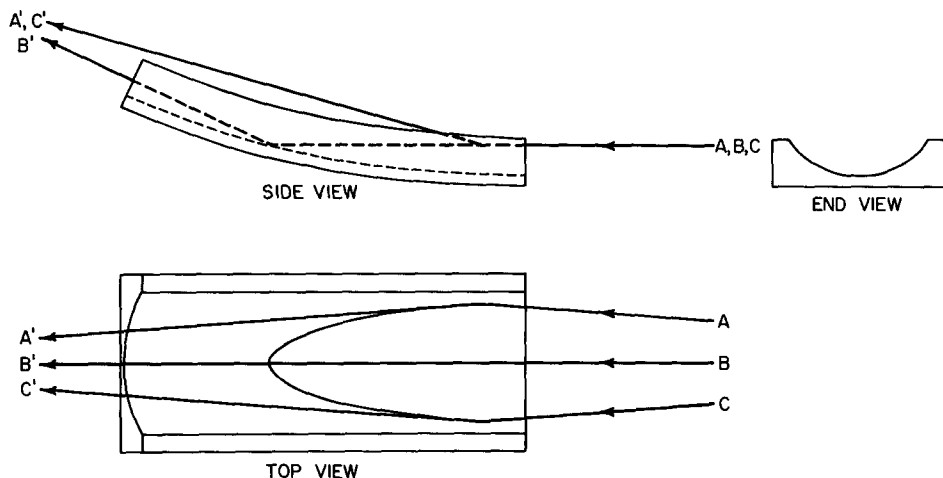
FIG. 7. Diagram of the effect of a toroidally bent focusing X-ray mirror on the energy resolution of synchrotron radiation. For this diagram, the X-ray beam incident on the mirror (rays A, B, C) is assumed to have only horizontal divergence. The effect of the mirror is to convert this horizontal divergence to vertical convergence in the reflected beam (rays A', B', C').

$$I = I_o\exp(-\mu x) \tag{9}$$

where I_0 is the intensity of X rays incident on the sample and I is the intensity transmitted. In general, measurement of the product μx is sufficient since the data usually are normalized to the edge jump. The detection equipment must then be able to give a quantity proportional to I_0 and one proportional to I. The transmission technique measures I_0 and I directly and $\ln(I_0/I)$ yields a quantity proportional to μx. Indirect techniques involve measurement of processes that are a result of the absorption of a photon rather than measurement of I directly. The fluorescence technique involves measurement of X-ray fluorescence (e.g., K_α emission for K-edge absorption) and this technique is used almost exclusively in biological applications.

    In the transmission and fluorescence techniques, detectors that generate output proportional to X-ray intensities are required. Two types are used: pulse (photon counting) detectors and dc (integrating) detectors.[19] Measurement of I_0 requires a resonably transparent detector so that the beam still strikes the sample. This is usually accomplished with a gas ionization chamber, a dc detector filled with an appropriate gas that can

[19] E. A. Stern, *AIP Conf. Proc.* **64,** 39 (1980).

be ionized by the X rays. The current thus generated across two charged plates is amplified and measured to be proportional to the X-ray intensity. The gas (e.g., He, Ne, N_2, Ar, etc.) is chosen to absorb an optimum fraction (~20–30%) of the radiation. For transmission work, the I detector should be chosen to absorb all the remaining photons. A larger ionization chamber often serves the purpose since it is generally useful to allow some residual radiation to pass through the I detector (for alignment purposes or for a simultaneous energy calibration measurement).

For detection of fluorescent photons, pulse detectors are commonly used (due to their better sensitivity at low count rates). In addition, pulse detectors allow some amount of energy discrimination (a factor important in fluorescence excitation measurements). In some cases, energy discrimination can also be achieved by using appropriate filters and this method has been used with both pulse detectors and gas ionization chambers in fluorescence detection experiments. Pulse detectors include gas proportional counters, scintillation counters, gas scintillation counters, and solid state detectors.

Data Acquisition

Transmission. Most biological samples (i.e., metalloproteins, metalloenzymes) are spectroscopically dilute and, as a result, fluorescence excitation techniques are used normally to collect XAS data. However, every EXAFS analysis requires data on "model compounds" for extraction of phase and amplitude information. (In this context, a model compound is defined as any structurally characterized metal complex with an appropriate absorber–scatterer pair.) XAS data on such compounds are almost always collected on solid samples using the transmission technique.

Figure 5 illustrates the simple setup required for transmission XAS data collection: a monochromator, an I_0 ionization chamber, some means to hold the sample, and an I ionization chamber. The sample usually rests on a remotely controlled y-z translation stage (defining x as the beam propagation direction) for easy alignment of the sample with the beam. The ionization chambers are filled with an inert gas chosen so that a certain fraction of the X-radiation is absorbed by the I_0 detector. The optimum fraction depends on the sample thickness and one can calculate the optimum sample thickness (x_{opt}) for best signal-to-noise ratio (S/N) to be[20]

[20] B.-K. Teo, *in* "EXAFS Spectroscopy, Techniques and Applications" (B.-K. Teo and D. C. Joy, eds.), p. 13. Plenum, New York, 1981.

$$\mu_t x_{opt} \approx 2.5 \tag{10}$$

where μ_t is the total absorption coefficient of the sample (just above the absorption edge of interest). (Note that the measurement of $\mu_t x$ is given by

$$\mu_t x = \ln \left(\frac{I_0}{I} \frac{I'}{I_0'} \right) \tag{11}$$

where I_0' and I' are measurements in the absence of the sample.) Given such a sample, the optimum fraction of the radiation absorbed by I_0 is 20–25%.[19,20] One can (crudely) adjust this fraction by putting different gases in the I_0 ionization chamber for different photon energies. It proves convenient to use N_2 for photon energies between ~6 and 12 keV and Ar for higher energies.

The optimum sample thickness in Eq. (10) should be considered a maximum—other experimental effects can lower the expected S/N. Such effects include beam instability, incorrect sample positioning, heterogeneous sample thickness (e.g., pinholes, etc.), harmonic contamination of the X-ray beam, and monochromator "glitches." The last two effects are treated in detail later. It is necessary to be extremely careful about making up solid samples, making sure the material is homogeneously ground and (usually) pressed. One can adjust $\mu_t x$ by using different thickness sample holders or by diluting the sample with an inert solid containing only low-Z atoms (BN, Li_2CO_3, and $LiBF_4$ are commonly used).

In most XAS measurements, the data are collected at discrete energies, selected by stepping motor positioning of the monochromator crystals to some Bragg angle, θ. It is necessary to use variable intervals (in stepping motor pulses, proportional to θ) since often much smaller steps are used across the edge. In the EXAFS region, both variable intervals and variable integration times are used often to compensate for the eventual k^n weighting of the processed EXAFS data. Thus, the scan is set up to collect data points equally spaced in k and the integration times are longer in the high-k region (to give constant S/N throughout the EXAFS region after multiplication by k^n). In practice, the total desired scan time precludes perfect compensation so that most reported EXAFS data still exhibit more noise in the high-k region.

The time used for collection of one spectrum (scan time) can vary anywhere from ~10 min to a few hours. The overhead time for (computer-controlled) movement of the monochromator stepping motor makes shorter scan times less efficient and (at SSRL) an effective lower limit is probably ~15–20 min. Due to spurious beam instabilities and the hazards associated with attempting to include shortened scans in the overall average, the upper limit of scan time is a function of the frequency of the beam
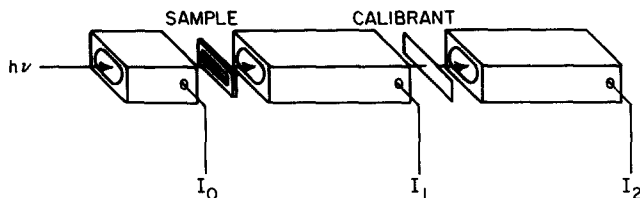
FIG. 8. Detector arrangement for measurement of internal calibration. The sample absorption is given by $\mu x = \ln(I_0/I_1)$ and the radiation that gets through the I_1 detector is used to measure the calibrant absorption, $\mu x = \ln(I_1/I_2)$.

problems. Since it is standard practice to discard the entire scan once a beam problem corrupts the data, if they are more frequent, the scan time should be shortened so that more complete scans can be acquired. At SSRL, an effective upper limit of ~1 hr seems reasonable, and an average scan time of ~30 min is common.

Energy calibration of the monochromator is generally accomplished by recording a high-resolution spectrum of the edge region of the appropriate metal foil. The inflection point of the absorption edge is used then for a single-point calibration. This is accomplished best by the internal calibration procedure illustrated in Fig. 8. A third ionization chamber is located behind the second with the calibrant between. Three measurements are recorded (I_0, I_1, I_2). A small amount of radiation passes through I_1, through the calibrant, and into I_2. The absorbance of the sample [$\mu_x x = \ln(I_0/I_1)$] is recorded simultaneously with the absorbance of the calibrant [$\mu_c x_c = \ln(I_1/I_2)$]. Thus each scan of the sample is calibrated internally simultaneously with data acquisition. This can be done for fluorescence excitation data as well, providing at least some radiation passes through the sample.

Fluorescence. For concentrated samples, the transmission technique is adequate. However, for spectroscopically dilute samples (as in most biological applications), the fluorescence excitation technique is the preferred method of data acquisition. In practice, for first-row transition metals, the lower limit of concentration for which transmission XAS is feasible is probably ~10 mM.[21]

The fluorescence XAS technique takes advantage of the fact that a certain fraction of the atoms from which a K-shell (1s) electron has been dissociated (by absorption of an X-ray photon) relax by emitting a fluorescent photon (see Fig. 9a). The fluorescent yield is a monotonically increasing function of atomic number. For example, K_α fluorescent yields

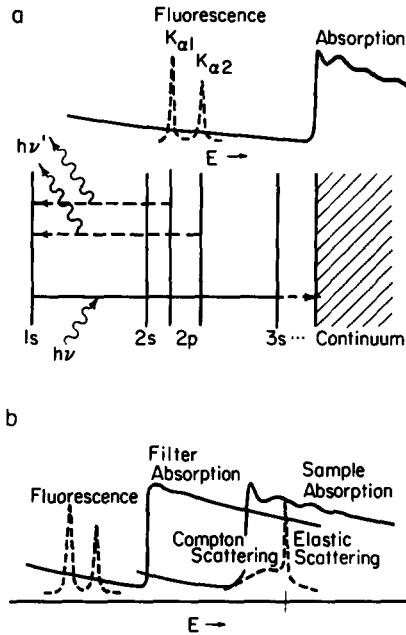[21] R. G. Shulman, P. Eisenberger, and B. M. Kincaid, *Annu. Rev. Biophys. Bioeng.* 7, 559 (1978).

FIG. 9. (a) General atomic energy level diagram illustrating K absorption and K_α fluorescence. The absorption and fluorescence spectra of the sample are shown above the energy level diagram. Measurement of the number of K_α photons fluoresced as a function of incident photon energy constitutes a fluorescence excitation spectrum. (b) The relationship of the filter absorption to the sample absorption, fluorescence, and scatter. The elastic and Compton scattering are shown for the particular incident photon energy marked on the abscissa. The filter is chosen so that it has a high absorption coefficient in the energy region of the scattered photons, but a low absorption coefficient in the energy region of the fluorescent photons. This is typically an elemental filter with atomic number one less than the absorbing atom (a "$Z - 1$" filter).

for Fe and Mo are 0.347 and 0.764, respectively.[20] The data collection proceeds in the same manner as for transmission XAS with the monochromator scanned through the energy range containing the sample absorption edge and EXAFS. However, instead of monitoring the transmitted intensity, the number of K_α photons emitted is measured (usually by photon counting techniques). This quantity is directly proportional to the number of photons absorbed and thus contains the same information. I_0 is still measured with a partially transparent ionization chamber and the signal of interest is F/I_0 (where F is the measured fluorescence signal). The advantage of the fluorescence technique for dilute (or thin) samples comes about due to the difference in energy of the K_α photons making up the signal and the photons making up the background (the elastic and

Compton scattered photons at higher energies). This is illustrated in Fig. 9b. The fluorescence technique gains sensitivity by making use of various scatter rejection schemes (i.e., being able to energy discriminate against scattered photons). This can be accomplished either by using detector systems with high-energy resolution or by choosing an appropriate low-pass filter which absorbs selectively the higher energy scattered photons (Fig. 9b). For study of an element with atomic number Z, an appropriate filter can be made from a thin foil or deposited layer of the element with atomic number $Z-1$.

There are four basic types of detectors that have been used for fluorescence-detected XAS work: scintillation counters,[22-25] solid-state detectors,[26] gas-filled detectors (either ionization chambers or proportional counters),[19] and the so-called "barrel monochromator."[27,28] Scintillation counters use a material that can convert photon-produced photoelectrons into electronic excitation energy which is discharged by emission of a visible or near-UV photon. A photomultiplier tube behind the scintillator detects this fluorescence. The most commonly used scintillators are NaI(Tl) or certain plastics. The advantage of scintillation counters is that they can reach fairly high count rates and they are inexpensive enough that arrays of detectors can be built[24,25] to cover a large solid angle (as high as $\sim 20\%$ of 4π) around the sample. The maximum count rate available to any photon counting detector is determined by its characteristic dead-time, τ. This is defined as the minimum time (Δt) which must separate adjacent pulses for each of them to be detectable. If $\Delta t < \tau$, the two pulses are counted as only one. Therefore, the observed count rate (N') is related to the actual count rate (N) by

$$N' = N(1 - N\tau) \qquad (12)$$

Equation (12) holds up to $N\tau \approx 0.4$.[19] Thus, *with* appropriate deadtime corrections, a detector will yield reliable count rates up to N_{max} where

$$N_{max} \approx 0.4/\tau \qquad (13)$$

[22] R. G. Shulman, P. Eisenberger, B.-K. Teo, B. M. Kincaid, and G. S. Brown, *J. Mol. Biol.* **124,** 305 (1978).

[23] E. A. Stern and S. M. Heald, *Rev. Sci. Instrum.* **50,** 1579 (1979).

[24] S. P. Cramer and R. A. Scott, *Rev. Sci. Instrum.* **52,** 395 (1981).

[25] J. C. Phillips, *J. Phys. E* **14,** 1425 (1981).

[26] J. Jaklevic, J. A. Kirby, M. P. Klein, A. S. Robertson, G. S. Brown, and P. Eisenberger, *Solid State Commun.* **23,** 679 (1977).

[27] J. B. Hastings, *in* "EXAFS Spectroscopy. Techniques and Applications" (B.-K. Teo and D. C. Joy, eds.), p. 205. Plenum, New York, 1981.

[28] M. Marcus, L. S. Powers, A. R. Storm, B. M. Kincaid, and B. Chance, *Rev. Sci. Instrum.* **51,** 1023 (1980).

For NaI (Tl) scintillation counters, the deadtime is ~ 1 μsec and $N_{max} \approx 4 \times 10^5$ cps. With plastic scintillators, the deadtime can be about an order of magnitude shorter[19] yielding another factor of 10 in maximum count rate. The main disadvantage of scintillation counters is the low energy resolution (no better than $\sim 50\%$ at 7 keV) which is not sufficient to separate K_α emission from scattering. Therefore, scintillation detector systems are generally used with appropriately designed filter assemblies.[23,24]

Solid-state detectors use semiconductor materials (Si or Ge) as ionization detectors. In some cases, to reduce the dark current of the semiconducting material, impurities are added (Li is most common) and the detector is operated at liquid nitrogen temperature. These detectors (most commonly SiLi or intrinsic Ge) have very good energy resolution (perhaps ~ 100 eV at 7 keV), but can operate only at a maximum of $\sim 20,000$ cps.[23] They also tend to be expensive and this (plus the liquid nitrogen dewars) makes it prohibitive to build an array to collect a significant solid angle of fluorescence.

The barrel monochromator[27,28] achieves its high-energy resolution by using Bragg reflection from graphite or LiF crystals to monochromatize the emitted radiation and using a Rowland circle geometry to focus a cone of rays from a point source (the sample) to a point on the detector (a solid-state detector was used in both reported systems). The crystals are formed (as a mosaic) into a concave "barrel" geometry in order to accomplish the focusing with monochromatization of the proper photon energy range (e.g., the FeK_α emission line). The main advantage of this system is its high-energy resolution, although this seems to be outweighed by the disadvantage of the small solid angle subtended ($\sim 1.5\%$ of $4\pi^{23}$) and the fact that a new crystal arrangement must be developed for use at each energy (e.g., one for Fe, one for Cu, etc.).

As with scintillation counters, gas-filled detectors (such as ionization chambers) have very poor energy resolution. Thus, for use as fluorescence detectors, a filter is virtually required (for dilute samples). In general, thicker filters give better scatter rejection but a point of diminishing returns is reached soon. This is due to the presence of filter fluorescence, produced by the absorption of scattered photons. As more scattered photons are absorbed by the filter, more filter fluorescence photons are produced and reach the detector, effectively generating more filter-transmitted scatter. This effect can be overcome partially by using baffles (known as Soller slits) which prevent a substantial amount of filter fluorescence (emitted in *all* directions by the filter) from reaching the detector. The Soller sites are designed to allow photons that originate at the sample to pass all the way to the detector unimpeded. Thus, depending upon the

profile of the sample "viewed" by the detector, the design of appropriate Soller slits can be quite complex.

The optimal arrangement for fluorescence detection studies on low-Z metals (e.g., Fe, Cu) has the sample at 45° to both the incident radiation and the fluorescence detector with the detector in the horizontal plane[29] (see Fig. 5). This not only allows the fluorescence detector to see an optimal projection of sample surface area, but also is the geometry which gives the minimum amount of background scatter. With an array of detectors, one packs the detectors around this particular orientation to collect as much solid angle as possible.[24] For XAS studies of higher-Z metals (e.g., Mo), one can use a sample with greater pathlength (up to ~ 1 cm of H_2O at 20 keV), still allowing transmission of some radiation for internal calibration, yet allowing more surface area of the sample to be "viewed" by the fluorescence detectors.

In general, the same (dedicated) minicomputer which controls the XAS experiment also takes care of data acquisition. Data from ionization chambers start out as current and go through a current preamplifier and a voltage-to-frequency converter in order to be recorded as cps. For scintillation counters, the individual pulses need to be amplified (by fast delay line amplifiers, for example) and then go through single channel analyzers (that allow discrimination against harmonic scatter) before being recorded as cps. For applications that use multiple detector arrays, the outputs of all the detectors can be summed in an analog fashion to give one signal (assuming the computer interface can handle the overall count rate), but for statistical reasons it is best to collect data from each channel (detector) separately and use an appropriate weighting scheme.[30]

Each channel will have a different S/N (depending on the specific electronic components and on the geometrical location of the detector) and in order to avoid overemphasizing the data from a channel with large scatter-to-fluorescence ratio, one should use a weighting scheme based on estimated S/N. The S/N for each channel can be estimated before data collection is begun by examining the actual data to get an estimate of the background and fluorescence counts and then assuming that photon statistics are obeyed. Figure 10 shows a hypothetical spectrum [of $(F/I_0)_i$ versus energy] which might be observed for the ith fluorescence channel. The signal of interest (e.g., the EXAFS) is assumed proportional to the size of the edge jump (measured as cps and normalized to I_0) and the noise

[29] D. R. Sandstrom and J. M. Fine, *AIP Conf. Proc.* **64**, 127 (1980).
[30] R. A. Scott, S. P. Cramer, R. W. Shaw, H. Beinert, and H. B. Gray, *Proc. Natl. Acad. Sci. U.S.A.* **78**, 664 (1981).
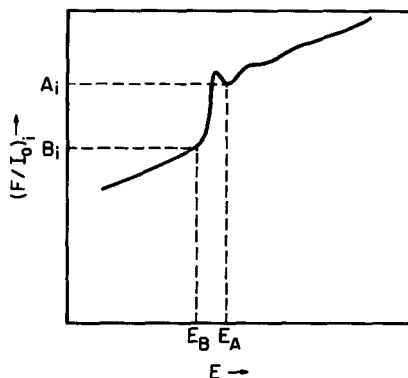
FIG. 10. Measurements used for calculation of weighting factors for fluorescence excitation spectra. The proper weighting factor can be calculated to be proportional to the relative edge jump [$\Delta_i' = (A_i - B_i)/A_i$].

is estimated (by photon statistics) as proportional to the square root of the total count rate (again normalized to I_0). For the ith channel, one need make only two measurements (see Fig. 10): a count rate (B_i) at an energy (E_B) just before the edge of interest and a count rate (A_i) at an energy (E_A) just after the edge of interest. Then the signal (S_i) and noise (N_i) for the ith channel are estimated as

$$N_i \propto A_i^{1/2} \tag{14}$$
$$S_i \propto (A_i - B_i) \equiv \Delta_i \tag{15}$$

The proper weighting factor (W_i) is proportional to the square of the S/N but also must include normalization of the data in the ith channel to unit edge jump (this is so that channels with equal S/N contribute equally to the weighted average edge jump):

$$W_i \propto \frac{(S_i/N_i)^2}{\Delta_i} = \frac{\Delta_i}{A_i} \equiv \Delta_i' \tag{16}$$

Thus, the proper weighting factors are just proportional to the relative edge jumps (Δ_i') in each channel. The properly weighted fluorescence ($\langle F \rangle$) is then calculated from the fluorescence in each channel (F_i) by

$$\langle F \rangle = \frac{\Sigma_i W_i F_i}{\Sigma_i W_i} \tag{17}$$

With the aid of the computer, the proper weighting may be done at the time of data acquisition. (This saves storage space since only one number is stored per energy.) However, in some cases, fluorescence detectors at

different locations respond differently to beam or monochromator instabilities (see below). Since it is difficult to know the extent of such behavior at data acquisition, it may be advantageous to postpone the proper averaging until the individual channels can be examined in detail.

Experimental Difficulties. The EXAFS oscillations that contain the desired structural information are a small modulation of a large signal. Measurement of EXAFS data is thus very sensitive to minor defects in sample or beam integrity. The mechanics of collecting EXAFS data is straightforward—the art is to be aware of possible artifacts and to know how to circumvent them. This section discusses a number of potential pitfalls, their causes, and possible solutions.

Especially for biological systems, sample integrity is of utmost importance. One must be able to demonstrate that the state (usually, oxidation state of the active site) of the sample is the same after EXAFS data collection as it was before. It is also desirable to have some evidence that this state existed *during* data collection (and was not just regenerated when the X rays were turned off). One solution is to do "on-line" monitoring of the sample in the X-ray beam.[31] This solution is complicated and expensive. It should suffice to perform the experiment at cryogenic temperatures, check the appropriate spectroscopic "handles" (usually EPR, but also perhaps optical reflectance) before and after data collection (also at cryogenic temperatures), and show that the XAS spectrum (both edge and EXAFS) does not change over the course of data collection.

The problem, of course, is that X-radiation is ionizing—hydrated electrons are easily produced by irradiation of aqueous solutions. It has been demonstrated that free radical EPR signals are observed in aqueous cytochrome *c* oxidase solutions after X-irradiation.[31–33] The danger exists that these hydrated electrons may diffuse to the metal active site(s), causing "photoreduction" or "radiation damage." Low temperatures (≤ 200 K) seem to alleviate the problem, since diffusion of the hydrated electrons to the metal sites at these temperatures becomes slower than radical recombination. At 77 K, in cytochrome *c* oxidase samples, the radiation-induced radicals disappear completely without significant reduction of the EPR-detectable metal sites in ~2 weeks.

Homogeneity of the physical state of the sample is also important if one is to avoid artifacts. This is of less importance in fluorescence data

[31] B. Chance, P. Angiolillo, E. K. Yang, and L. Powers, *FEBS Lett.* **112**, 178 (1980).

[32] G. W. Brudvig, D. F. Bocian, R. C. Gamble, and S. I. Chan, *Biochim. Biophys. Acta* **624**, 78 (1980).

[33] R. A. Scott, *in* "The Biological Chemistry of Iron" (H. B. Dunford, D. H. Dolphin, K. N. Raymond, and L. C. Sieker, eds.), p. 475. Reidel Publ., Boston, Massachusetts, 1982.

collection. For example, frozen solutions (not glasses) can *usually* be examined by fluorescence with no problems, but transmission experiments on such physically heterogeneous samples are not possible. For transmission work, any portions of the sample that are more transparent to X rays (e.g., thin spots, bubbles, pinholes, cracks) will increase the I ionization chamber reading above what it should be yielding a lower $\ln(I_0/I)$ quantity. Assume that some fraction, f, of the sample is thinner than the rest (of thickness x) by an amount, δ (i.e., the thin spots have thickness $x - \delta$). Then the measured signal would be

$$(\mu x)_{\text{meas}} = \ln(I_0/I) = \mu x - \ln\{1 - f[1 - \exp(\mu\delta)]\} \qquad (18)$$

[instead of $\ln(I_0/I) = \mu x$, for a homogeneous sample of thickness x]. This signal is no longer proportional to μx, the result being that the normalized EXAFS amplitude will be underestimated. For example, if $\mu x = 2.5$ [the optimum thickness given in Eq. (10)], 1% of the illuminated surface area of the sample consists of pinholes (or cracks) with $\delta = x$, and the edge-to-background ratio is 4, the EXAFS amplitude would be underestimated by ~4%. Worse yet, if the experiment does not track the vertical motion of the beam perfectly during the scan, the percentage of radiation that "leaks" through the pinholes will change, giving rise to small discontinuities in the data.

For fluid solution samples, these problems can be overcome by assuring that the solution is well mixed and that no bubbles are in the path of the X-ray beam. For solid samples, the material should be extensively ground with a mortar and pestle and pressed into a spacer (usually with Mylar or Kapton windows) to form a flat, homogeneous pellet.

Even with perfectly homogeneous samples, transmission experiments can be affected by beam artifacts. With synchrotron radiation, these can be of two types: (1) spurious, time-dependent changes in the synchrotron radiation beam; and (2) artifacts introduced or emphasized by the optics (i.e., the monochromator). The first category includes sudden changes in beam intensity, beam density, or beam position. Any of these are manifested as a sudden drop in I_0 reading. These discontinuities are usually reflected in the measured $\ln(I_0/I)$ quantity due to the fact that I_0 and I usually do not ratio perfectly (vide infra). Such artifacts are infrequent, are easy to spot, and are usually out of the experimenter's control.

The second category of beam artifacts are a direct result of the double flat crystal monochromators used for XAS. The presence of n in the Bragg relationship, Eq. (7), results in contamination of the reflected beam (supposedly just the fundamental, $n = 1$) with higher harmonics ($n = 2, 3,...$). For example, a monochromator set to reflect 10 keV X rays also reflects 20 keV X rays (along precisely the same path). Of course, the absorption

coefficient of the sample for the higher energy radiation is much lower than for the fundamental. Thus, most of this harmonic radiation "leaks" through the sample (it is often called leakage radiation) causing the same type of distortion of the EXAFS data as leakage of the fundamental through pinholes. (This is usually referred to as the "thickness effect" since the distortion is worse for thicker samples.[34–38]) If the detectors could discriminate against this leakage radiation, it would not be a problem, but ionization chambers have very poor energy resolution. Thus, it is typically the presence of this leakage radiation which causes I_0 and I to ratio imperfectly. This in turn causes spurious beam fluctuations to show up in $\ln(I_0/I)$.

Another artifact introduced by the double crystal monochromators is the so-called monochromator "glitch." In addition to the set of Bragg planes being used for fundamental reflection, there are many others that may reflect some of the fundamental intensity in another direction at precise energies in the scan. This is registered as a sharp dip in the I_0 reading which occurs at the same energy all the time (i.e., every scan) and is referred to as a "glitch." Again, due to imperfect ratioing (from leakage radiation), this sharp "glitch" shows up as a positive spike in the $\ln(I_0/I)$ data.

It is clear from the above discussion that leakage radiation can introduce subtle distortions to the resulting EXAFS data that must be minimized. To avoid distortions due to the thickness effect, one should be sure to make samples that are thinner or more dilute so that the distortions are not as large. However, this is merely treating the symptoms. The preferred method of solving all such problems is to reduce or eliminate the leakage radiation present in the beam. The most direct method of harmonic discrimination (assuming that the harmonic is the source of leakage radiation) is adjustment of the source spectrum to decrease the *relative* amount of higher energy photons present. For laboratory sources, one can just turn down the power on the X-ray tube, while for synchrotron radiation, one must choose to run at lower electron energy (shifting the source spectrum to lower critical energy), or turn down a wiggler magnet field (if applicable). In any case, some sacrifice in fundamental intensity is necessary.

[34] S. M. Heald and E. A. Stern, *Phys. Rev. B: Solid State* [3] **16**, 5549 (1977).
[35] D. M. Pease, L. V. Azaroff, C. K. Vaccaro, and W. A. Hines, *Phys. Rev. B: Condens. Matter* [3] **19**, 1576 (1979).
[36] E. A. Stern, S. M. Heald, and B. A. Bunker, *Phys. Rev. Lett.* **42**, 1372 (1979).
[37] E. A. Stern, B. A. Bunker, and S. M. Heald, *Phys. Rev. B: Condens. Matter* [3] **21**, 5521 (1980).
[38] E. A. Stern and K. Kim, *Phys. Rev. B: Condens. Matter* [3] **23**, 3781 (1981).

Another method is to choose a set of Bragg planes for which the harmonic reflection is forbidden. For example, with Si[111] crystals, the even order harmonics (e.g., Si[222], Si[444]) are nearly forbidden. This method is not always available for a particular experiment. One of the most commonly used methods of harmonic discrimination is monochromator "detuning." This method takes advantage of the relatively narrow rocking curve of the harmonic (compared to the fundamental). Detuning refers to rotating one of the monochromator crystals (with respect to the other) slightly out of parallel alignment. Detuning slightly off the rocking curve maximum will reduce drastically the amount of harmonic reflected while affecting only slightly the reflected fundamental intensity.

A slightly more drastic approach (to achieve harmonic discrimination) is to condition the source spectrum before the radiation reaches the monochromator by the use of X-ray reflecting optics. In the X-ray region, total external reflection from a material occurs only at glancing angles (below some critical angle).[39] This critical angle depends on photon energy; the higher the energy, the smaller the critical angle. Thus, with proper choice of material and incident angle, one can design an X-ray mirror which will reflect the fundamental but absorb the harmonic. One can use a flat mirror provided a material with adequate optical flatness is available (float glass has been used for this purpose), Platinum- (or gold-)coated fused quartz has been used in mirrors designed for X-ray focusing applications. Although the mirror shown in Fig. 7 was designed to gather a wide horizontal acceptance and focus it into a bright spot at the sample, a secondary effect is very good harmonic discrimination (when the harmonic is above the cutoff energy defined by the angle of the mirror).

In the absence of leakage radiation, distortion of the EXAFS data (i.e., underestimation of EXAFS amplitudes) can also be caused by detector nonlinearity. For transmission data, the I ionization chamber observes a signal which varies over a much wider dynamic range (due to the sample absorption edge) than the I_0 signal. If the I detector has a nonlinear response, the effect will resemble closely the leakage radiation effect (before the edge, the I reading will be high, in a nonlinear region, and will be measured as smaller than it really is; after the edge, the I reading decreases into a linear region and is measured correctly). Fortunately, ionization chambers exhibit extremely linear response, but if other kinds of detectors are used, their linearity should be checked (against an ionization chamber, for example).

Fluorescence detectors can also exhibit nonlinear behavior [as described by their inherent deadtime as in Eq. (12)]. Thus, if fluorescence

[39] R. C. Gamble, *AIP Conf. Proc.* **64**, 113 (1980).

detectors are operated near their high count rate limit, distortions will occur again since the fluorescence signal will get considerably larger after the sample absorption edge. Deadtime corrections can correct this problem partially but only up to a certain limit [Eq. (13)]. The best solution is to use fluorescence detectors well below their saturation limit.

Just as with leakage radiation, detector nonlinearity will result in imperfect ratioing of I_0 and I. Along with this comes susceptibility to monochromator "glitches," spurious beam fluctuations, etc. For an ideal XAS experiment, one should assure that all detectors are operating in a linear range and that effective harmonic discrimination is used.

Data Reduction and Analysis

Collecting the data is only half of what is required to use EXAFS successfully to determine the structure of a metal site. Reduction and analysis of the data are at least as important and can be as susceptible to artifacts as data acquisition. It is convenient to divide the data workup into two steps: (1) data reduction involves extraction of the EXAFS data from the raw XAS data; (2) data analysis involves extraction of the structural information from the EXAFS data (by curve-fitting).

Data Reduction. The raw data as acquired consist of I_0, I, and possibly F (fluorescence) data as a function of monochromator motor steps. (If the internal calibration method was used, another "I_2" column corresponding to the third ionization chamber will also be present.) If more than one fluorescence detector was used, the fluorescence data may be in separate columns (channels), F_i. If this is the case, the F_i should be properly averaged within each scan (each data file) before any further processing occurs. The proper averaging consists of weighting the fluorescence channels appropriately based on their individual S/N (as discussed above). However, it is often useful to carry each F_i column individually through the data reduction and compare the EXAFS of each column to determine whether there are F_i columns that are too noisy to keep in the average. Once this is determined, the proper weighted average of the selected F_i columns can be done and the data reduction can proceed with the averaged fluorescence data, $\langle F \rangle$.

The next sept in data reduction (or the first step if transmission data is being used) is to convert monochromator motor steps into electron volts (eV). A single-point calibration is generally used to perform this conversion. With the external calibration procedure, separate scans of the appropriate metal foil should be recorded before and after the sample data. The $\ln(I_0/I)$ data from these scans give the calibrant edges which must be analyzed to locate the inflection point. With the internal calibration

method, each sample data file has the calibrant spectrum as $\ln(I/I_2)$. In either case, the inflection points are located by finding all of the downgoing zero-crossings in the second derivative of the edge spectrum. The first inflection point in each metal edge corresponds to the tabulated energies in the periodic table of Fig. 1. Assuming that the motor step positions of all the calculated inflection points are approximately equal, they can be averaged to give the calibration point, S_c (in motor steps). The energy, E_c, corresponding to this is taken from the table (Fig. 1) and the energy, $E(i)$, for the ith point in each spectrum is calculated by

$$E(i) = hc/2d \sin \theta(i) \tag{19}$$

$$\theta(i) = \theta_c + [S(i) - S_c]/\Delta \tag{20}$$

$$\theta_c = \sin^{-1}(hc/2dE_c) \tag{21}$$

where d is the monochromator crystal d-spacing, $S(i)$ is the motor step value for the ith data point, and Δ is the number of motor steps per degree of monochromator crystal rotation.

Usually, at the same time the energy scale is generated a k-scale (k is the photoelectron wave vector, in Å^{-1}) and the appropriate ratioed data can also be generated. $k(i)$ is calculated for each $E(i)$ using Eq. (1). In order to perform this calculation, one must choose a threshold energy, E_0, which is not a trivial matter. For a particular absorber, E_0 is expected to depend upon the valence state, but it cannot be chosen to match the inflection point of the sample absorption edge because bound state transitions may influence this quantity. The usual approach is to arbitrarily pick an E_0 for a particular absorber or use the measured inflection point and then allow E_0 to vary (redefining the k-scale) during curve-fitting. The ratioed data will be $\ln(I_0/I)$, (F_i/I_0), or $(\langle F\rangle/I_0)$. Once these ratioed data are generated, plots of each data file (each scan) can be examined to determine whether any need to be discarded (e.g., if they were not finished, too noisy, or contained beam artifacts). The remaining good scans can then be averaged together and the EXAFS data will be extracted from this averaged XAS spectrum.

The next step in data reduction is the subtraction of the background from the edge and EXAFS. For transmission data, this background is due to absorption by all the other (lower atomic number) elements in the sample plus residual absorption due to the lower energy edges of the element being studied (e.g., if the Cu K edge is being examined, the Cu L edges will contribute to the background). For fluorescence data, the background consists of any scattered intensity not removed by the scatter rejection scheme (e.g., the filters). In general, the procedure is to con-

struct a smooth curve (a polynomial of low order, $-2 \leq n \leq 3$) which mimics the background as well as possible.

Four methods may be useful. (1) Measure the background using an appropriate sample and fit it with a polynomial. This works well for fluorescence data for which a sample of buffer can mimic the scatter background reasonably well. For transmission data, however, it is extremely difficult to generate a sample containing all the appropriate elements except the metal. (2) Fit the sample data in the preedge region and extrapolate it through the edge and EXAFS regions. This may be successful with either transmission or fluorescence data, but caution must be exercised since the extrapolation is over a wider energy range than is actually fit and it is not guaranteed to mimic the background. (3) Fit the sample data in the EXAFS region (starting ~50 eV above the edge) with a polynomial and subtract a constant from it to force it through the data just before the edge. This approach can work for either transmission or fluorescence data. The polynomial is not guaranteed to mimic the background well, but it will level out the data in the EXAFS region, making the spline fit easier (vide infra). (4) For transmission data, one can use the Victoreen formula[40] to estimate the background (given the elemental composition of the sample). The Victoreen formula is given by

$$\mu = C\lambda^3 - D\lambda^4 \tag{22}$$

where λ is the X-ray wavelength and C, D are tabulated coefficients.[40] Each element has two sets of coefficients (one set for before the element's absorption edge, one for after) and the calculated Victoreen must be summed for each element in the sample, then multiplied by a factor, γ (related to the unknown thickness and concentration of the sample), to force it through the sample data just before the edge.

The selection of background to subtract may seem rather arbitrary. It is important to realize that the exact nature of this curve is not critical to the data reduction. In principle, the raw data [denoted F_0, but could be $\ln(I_0/I)$ or (F/I_0)] can be written as

$$F_0 = \gamma\mu + F_{\text{back}} \tag{23}$$

where γ is a proportionality constant (related to concentration, sample thickness, fluorescence yield, etc.) and F_{back} represents the background. Ideally, the procedure described above would find a perfect model of F_{back} and subtraction would give the signal, F_1:

[40] C. H. MacGillavry and G. D. Rieck, eds., "International Tables for X-Ray Crystallography," Vol. III, p. 171. Kynoch Press, Birmingham, England, 1968.

$$F_1 \equiv (F_0 - F_{back}) = \gamma\mu \qquad (24)$$

Ultimately, we want to extract the EXAFS data (χ), which is theoretically represented by

$$\chi \equiv \frac{\mu - \mu_0}{\mu_0} \qquad (25)$$

where μ_0 is the absorption expected for a free atom. In our ideal case, γ is known and the next step in data reduction would involve subtracting and normalizing F_1 with the function $\gamma\mu_0$:

$$F_2 \equiv (F_1 - \gamma\mu_0)/\gamma\mu_0 = \chi \qquad (26)$$

Unfortunately, in the real world, F_{back} can never be perfectly modeled and γ is an unknown. The procedure described above yields some imperfect approximation to F_{back} (defined as F'_{back}) and subtraction yields

$$F'_1 \equiv (F_0 - F'_{back}) = \gamma\mu + \Delta F \qquad (27)$$

where $\Delta F \equiv (F_{back} - F'_{back})$. In this nonideal case, the background is not completely removed and the next step which should involve subtraction of the scaled atomic absorption coefficient ($\gamma\mu_0$) will not work.

However, the appropriate function to subtract can be found by simply fitting the EXAFS region (after background subtraction) to a smooth curve, μ_s. This is usually accomplished by the use of a polynomial spline. Typically, the EXAFS region is broken up into two or three spline regions and each region is fit with a polynomial (of third order, for example). The spline criteria are that the polynomials meet at the region endpoints with equal value and equal slope. This calculation of μ_s is found to be generally useful for both transmission and fluorescence data. Care must be exercised so that (1) μ_s does not track any EXAFS oscillations, thus eliminating them; and (2) there is no low frequency curvature left in the EXAFS data after subtraction of μ_s. Point (1) is usually not a problem as long as the spline polynomial order is low enough (third order is almost always sufficient) and the number of spline regions is not too large (no more than four regions are needed). Point (2) causes a problem only when μ_s does not fit the "background" curvature in the EXAFS region. This is the reason for the F'_{back} subtraction; it gives an F'_1 which is reasonably level (except for the EXAFS oscillations) and usually allows the spline to fit the overall curvature more precisely. It is also possible to check for an improper spline fit by looking for artifactual low-frequency peaks in the Fourier transform (vide infra).

The assumption in the above discussion is that the spline fit takes care of both the atomic falloff and the residual background:

$$\mu_s = (\gamma\mu_0 + \Delta F) \tag{28}$$

and the spline subtraction then yields

$$F'_1 - \mu_s = \gamma(\mu - \mu_0) \tag{29}$$

All that remains is to normalize the data to the atomic falloff and the result will be the EXAFS. The proper normalization function (N) is the atomic falloff [as modeled by the Victoreen formula, Eq. (22)] scaled so that the atomic absorption has an edge jump identical to the F'_1 data:

$$N = \gamma\mu_0 \tag{30}$$

$$\chi = (F'_1 - \mu_s)/N \tag{31}$$

In general, χ is treated as a function of **k**, the photoelectron wave vector, rather than a function of energy [the theoretical EXAFS expression, Eq. (2), is written as a function of **k**]. $\chi(\mathbf{k})$ is severely damped in **k**-space, yet much information is contained in oscillations at high **k**. $\chi(\mathbf{k})$ is usually weighted by some power of **k** (k^3 is now almost universal) in displayed EXAFS and in curve-fitting to compensate for this damping. [Note that some EXAFS spectra were and may still be displayed as $k^n\chi(\mathbf{k})$ with $n = 0, 1, 2$. Care must be exercised to know what is being plotted before comparisons of literature spectra can be done.]

Data Analysis. The data reduction procedures summarized above have succeeded in extracting the EXAFS data, $\chi(\mathbf{k})$, from the raw XAS data. The data analysis procedures to be discussed in this section are designed to interpret these EXAFS data in terms of structural information concerning the metal site. Data analysis may be treated on different levels: qualitative information may be obtained by examining the Fourier transform (FT) of the EXAFS data; quantitative information may be extracted by the use of curve-fitting techniques. Both of these approaches will be described here.

EXAFS data are normally displayed in **k**-space and since **k** has units of Å^{-1}, a Fourier transform will yield transform data in the inverse space, having units of Å. This is real space (with units of distance) but the transform is *not* a true radial distribution function. Instead, the inverse space will be defined here as R'-space, where R' is related to R (the true distance from the absorbing atom) by

$$R' = R + \alpha_1 \tag{32}$$

where α_1 is a (linear) phase shift. In general, the FT is carried out using

$$F(R') = \int_{\mathbf{k}_{min}}^{\mathbf{k}_{max}} \mathbf{k}^n\chi(\mathbf{k})\exp(2i\mathbf{k}R')d\mathbf{k} \tag{33}$$

The resultant $F(R')$ is a complex function of R' with both real and imaginary components, k_{min} and k_{max} are the limits used to select the $\chi(k)$ data to be included in the transform (k_{min} is usually chosen to be ~ 4 Å^{-1}), and k^n reflects the weighting of the $\chi(k)$ data as already discussed (usually, $n = 3$). Of course, with discrete $\chi(k)$ data, the integral of Eq. (33) must be done numerically using, for example, a Simpson's rule approach.[41]

Since the $\chi(k)$ function is assumed to be only real, the $F(R')$ function is required to be a symmetric function. However the only physically useful data are those for which $R' > 0$. Typically only the modulus of the FT is plotted (as shown in Fig. 11). This is given by Eq. (34):

$$|F(R')| = \{[F_{re}(R')]^2 + [F_{im}(R')]^2\}^{1/2} \tag{34}$$

Each term in the EXAFS summation of Eq. (2) gives rise to a characteristic sine wave, which in turn gives rise to a single peak in the FT. Thus, observation of a peak in the $F(R')$ data suggests the presence of a shell of atoms in the EXAFS. Care needs to be taken since small peaks appear in the FT due to truncation of the $\chi(k)$ data and due to noise. Thus, only FT peaks larger than some baseline may be interpreted properly as true shells of atoms. This baseline may be approximated by using the height of peaks in the "high-frequency" (large R') portion of the $|F(R')|$ data (see Fig. 11).

For a shell of atoms at distance R_{as} from the absorbing atom, $|F(R')|$ will exhibit a peak centered at $R' = R'_{as}$, where R'_{as} is related to R_{as} by Eq. (32). The phase shift (α_1) occurs because the EXAFS expression [Eq. (2)] is *not* a sum of simple sine waves. In particular, $\alpha_{as}(k)$ is k dependent and may be approximated as a polynomial in k:

$$\alpha_{as}(k) \approx a_0 + a_1 k + a_2 k^2 + \cdots \tag{35}$$

Thus, the sine term of Eq. (2) may be written

$$\sin[(2R_{as} + a_1)k + a_0 + a_2 k^2 + \cdots]$$

and the frequency is really given by $(2R_{as} + a_1)$. In the FT described by Eq. (33), the 2 has been factored out and thus $R'_{as} \approx R_{as} + a_1/2$ is the peak position in the $|F(R')|$ data ($\alpha_1 \approx a_1/2$). For many different types of scatterers, α_1 takes on values ranging from ~ -0.5 to ~ -0.2 Å.

If each shell gave rise to a simple sine wave in $\chi(k)$, one would also expect delta functions in the $|F(R')|$ data. Thus, the k dependence of α_{as} also contributes to broadening of the FT peaks. The peak widths contain an additional contribution from the overall shape of the amplitude envelope for that shell. This comes both from the inherent backscattering

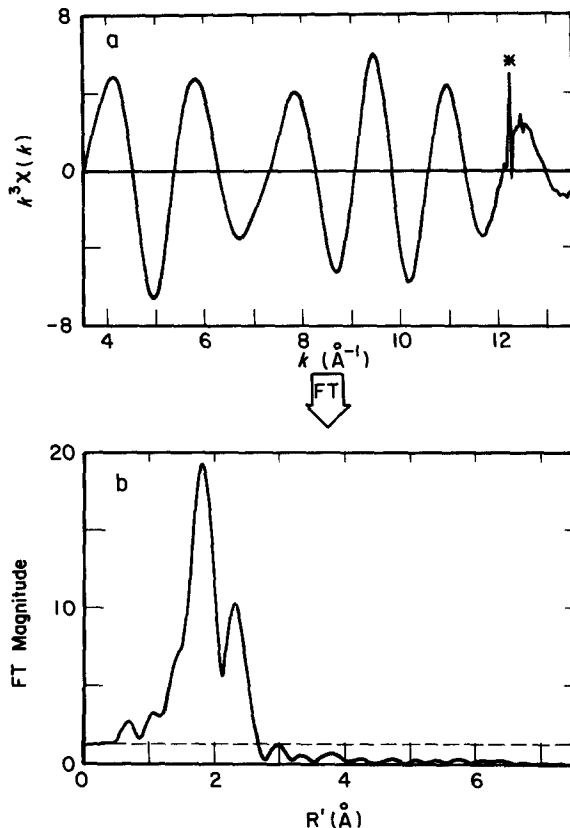[41] P. A. Stark, "Introduction to Numerical Methods," p. 202. Macmillan, London, 1970.

FIG. 11. Example of Fourier transformation. (a) Fe EXAFS data of $(NEt_4)_2$ [$Fe_4S_4(t$-BuS)$_4$ (the sample was a gift from K. Hagen and R. H. Holm), plotted as $k^3\chi(k)$ vs k. The beat pattern indicates more than one shell of atoms around the Fe. The asterisk marks a monochromator glitch. (b) The result of Fourier transformation [using Eq. (33)] of the Fe EXAFS data in (a) over the range $k = 3.5–13.5$ Å^{-1}. Mathematically, the two major FT peaks observed are the result of the beat pattern in (a). Physically, the peak at 1.85 Å is assignable to Fe–S scattering and the peak at 2.34 Å is due to Fe–Fe scattering. The dashed line indicates the approximate noise level in this FT.

amplitude, $B_s|f_s(\pi,\mathbf{k})|$, and from the Debye–Waller factor, $\exp(-2\sigma_{as}^2\mathbf{k}^2)$. Larger σ_{as} values give rise to broader FT peaks, so that data collection at lower temperatures gives rise to smaller σ_{as}, yielding sharper FT peaks. In some instances, FT peaks at high R' can be brought out of the noise by lowering the temperature of data collection.

Given the ability to account for variations in σ_{as} from one sample to another, the area of an FT peak can be used as a measure of N_s, the number of scatterers in the shell. It is often difficult, however, to glean any independent information concerning the value of σ_{as} and determina-

tions of N_s are therefore susceptible to large errors. Thus, FT peak heights (or areas) can be used only for crude estimations of relative numbers of atoms. Some methods of curve-fitting analysis will be described below to address this problem.

One other utility of Fourier transformation should be mentioned. This involves a technique known as Fourier filtering. A certain region of $F(R')$ may be selected and backtransformed to k-space. If the selected region includes all of the important FT peaks, but not the high-R' region of $F(R')$ (which presumably consists solely of noise), then the result of backtransformation is the $\chi(\mathbf{k})$ data with all the high-frequency noise filtered out. Alternatively, the selected portion of $F(R')$ may contain a single peak, in which case the backtransformed data consist of the contribution of a single shell to $\chi(\mathbf{k})$. In this manner, it may be possible to extract out the individual "sine" waves that make up the $\chi(\mathbf{k})$ data. Initial curve-fitting may then be performed on this single shell. Figure 12 shows an example of each of these filtering techniques.

For curve-fitting analysis, it is necessary to know the amplitude and phase of the photoelectron backscattering function for the particular absorber–scatterer pair under consideration. In Eq. (2), these are represented by $B_s|f_s(\pi,\mathbf{k})|$ and $\alpha_{as}(\mathbf{k})$, respectively. Different methods exist for obtaining these functions and these methods will be discussed in detail below. One of these methods involves complex backtransformation[21,42] of a single peak in the $F(R')$ data. Selection of the appropriate portion of $F(R')$ is usually done by multiplying $F(R')$ by a window function consisting of zeroes outside the R' range of interest. The window function is typically unity in the desired R' region, but is preferably shaped so that a smooth transition from unity to zero occurs on each side of the selected FT peak. A typical shape function is a half-Gaussian and the window shown in Fig. 12c is a function made up of two half-Gaussians, each with 0.15 Å HWHM (half width at half maximum).

If we define $F_w(R')$ to be $F(R')$ multiplied by the appropriate window function, the complex backtransform may be described by the integral

$$\mathbf{k}^n\chi'(\mathbf{k}) = \frac{2}{\pi} \int_{R'_{min}}^{R'_{max}} F_w(R')\exp(-2i\mathbf{k}R')\,dR' \tag{36}$$

In this expression, $\chi'(\mathbf{k})$ represents the filtered EXAFS (a complex quantity) and R'_{min} and R'_{max} are selected to include all of the nonzero points in the windowed $F_w(R')$ data. The resultant $\chi'(\mathbf{k})$ data are typically useful only over the original k-space region used for the forward transform ($\mathbf{k}_{min}$

[42] P. A. Lee, P. H. Citrin, P. Eisenberger, and B. M. Kincaid, *Rev. Mod. Phys.* **53**, 769 (1981).
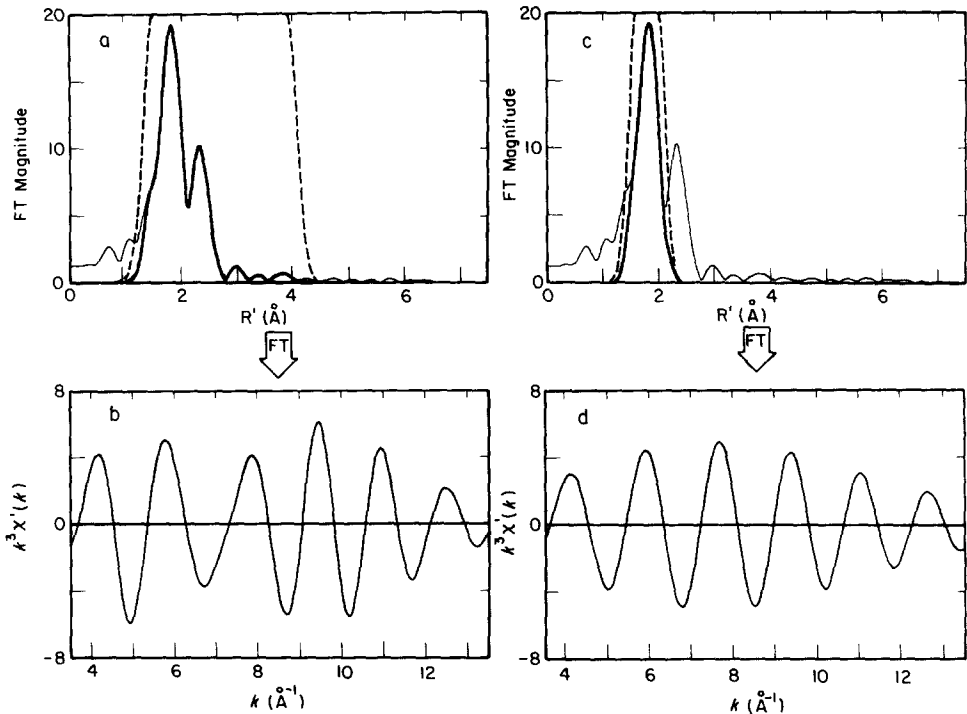
FIG. 12. Examples of Fourier filtering. In both (a) and (c), the dashed line is the filter window and the bold line is the product of this window and the Fourier transform, i.e., the data to be backtransformed. The results of transformation [using Eq. (36)] of the data in (a) and (c) are given in (b) and (d), respectively. The $\chi'(k)$ data in (b) are the result of "noise filtering" of the $\chi(k)$ data of Fig. 11a (note the absence of the monochromator glitch in Fig. 11a). The $\chi'(k)$ data in (d) are the result of extraction of the Fe–S shell (the 1.85 Å FT peak) from (c).

to k_{max}). The real and imaginary components of $\chi'(k)$ over this region can be used to form the following functions:

$$A(k) = |\chi'(k)| = \{[\chi'_{re}(k)]^2 + [\chi'_{im}(k)]^2\}^{1/2} \tag{37}$$

$$\Phi(k) = \tan^{-1}[\chi'_{im}(k)/\chi'_{re}(k)] \tag{38}$$

These functions are components of an EXAFS expression of the form

$$\chi'(k) = A(k)\sin[\Phi(k)] \tag{39}$$

An example of extraction of $A(k)$ and $\Phi(k)$ is given in Fig. 13. Comparison of Eq. (39) with Eq. (2) indicates that $A(k)$ is related to the backscattering amplitude and $\Phi(k)$ to the backscattering phase of the absorber–scatterer pair giving rise to the selected FT peak:
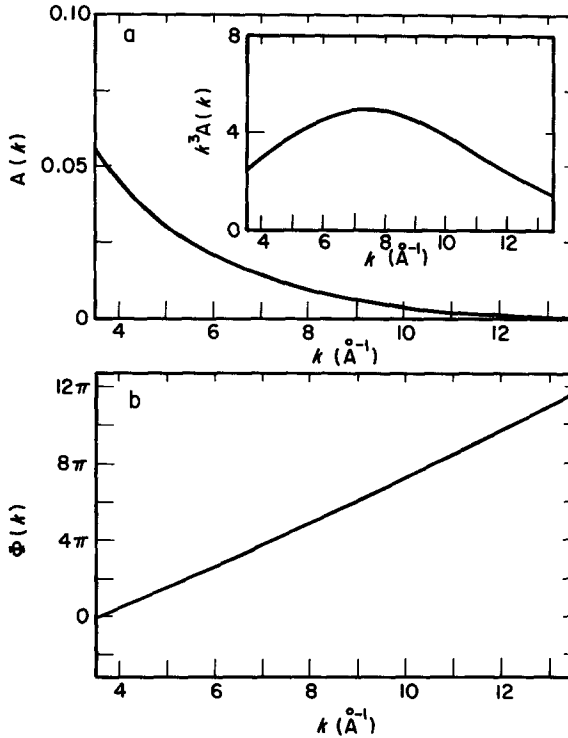
FIG. 13. The functions $A(k)$ and $\Phi(k)$ extracted [by complex backtransform, Eqs. (37), (38)] from the Fe–S shell (the data in Fig. 12c and d). The inset to (a) is the k^3-weighted $A(k)$ function which constitutes the amplitude envelope of the $k^3\chi'(k)$ data of Fig. 12d.

$$A(k) = \frac{N_s B_s |f_s(\pi,k)|}{kR_{as}^2} \exp(-2\sigma_{as}^2 k^2) \qquad (40)$$

$$\Phi(k) = 2kR_{as} + \alpha_{as}(k) \qquad (41)$$

[One should note that, in practice, the complex backtransform technique for determining $A(k)$ is unique, but the determination of $\Phi(k)$ by Eq. (38) is subject to some ambiguity. $\Phi(k)$ should be a monotonically increasing function, dominated by $2kR_{as}$, but the $\tan^{-1}$ function has discontinuities. Thus, the calculated $\Phi(k)$ data must have $n\pi$ added to it periodically. Also, the form of the Fourier transform equations used herein introduces a sine/cosine ambiguity so that $\pm\pi/2$ must be added to the calculated $\Phi(k)$, depending on the quadrant $\Phi(k)$ starts in, for $\chi'(k)$ to mimic the $\chi(k)$ data properly.]

The most important part of EXAFS data analysis is the curve-fitting of the EXAFS data, which allows interpretation of the EXAFS oscillations in terms of the actual structure around the absorbing metal atom. The general curve-fitting approach involves hypothesis of a local structural environment (involving types and numbers of atoms at given distances from the metal), followed by calculation of the EXAFS spectrum expected for this proposed structure, and comparison of this simulated EXAFS with the observed data. Typically, some sort of optimization procedure is used to alter the details of the proposed structure until the simulated EXAFS best fits the observed data according to a least squares criterion. Relating this to the EXAFS expression of Eq. (2), selection of the scatterer type (i.e., atomic number, Z) corresponds to generating the functions $B_s|f_s(\pi,\mathbf{k})|$ and $\alpha_{as}(\mathbf{k})$ (by methods yet to be described). Then, for each shell, initial values for the parameters R_{as}, N_s, and σ_{as} are chosen and the optimization consists of varying any or all of these parameters until the best least-squares fit is obtained. In some optimization procedures, the $\mathbf{k}$-scale may also be optimized by varying a parameter called ΔE_0 (for each shell) which corresponds to a difference in the ionization threshold energy for different shells.

The difference among the various methods of curve-fitting originate in different methods for generating the necessary amplitude and phase functions [$B_s|f_s(\pi,\mathbf{k})|$ and $\alpha_{as}(\mathbf{k})$] for a given absorber–scatterer pair. Two basic methods are available: *ab initio* calculation of theoretical amplitude and phase functions and empirical measurement of amplitude and phase functions using measured EXAFS data on structurally characterized ("model") compounds.

Theoretical amplitude and phase functions are tabulated (for most elements) from $\mathbf{k} \approx 4.0$–15.0 Å^{-1} by Teo and Lee.[43] The phase functions depend upon the E_0 value used to extract the EXAFS data, so that curve-fitting with theoretical functions usually also involves optimization of ΔE_0. Although the theoretical phase functions seem to match experiment fairly well (given the proper choice of E_0), the theoretical amplitude functions often predict the EXAFS to be larger than observed (by a factor of ~2) and thus, require the use of the scale factor, S_s, of Eq. (6). Teo and co-workers have developed a modified curve-fitting approach known as the FABM (fine adjustment based on models) method[44] for using structurally characterized compounds to calculate appropriate values for S_s (and ΔE_0).

The empirical approach to generating amplitude and phase functions

[43] B.-K. Teo and P. A. Lee, *J. Am. Chem. Soc.* **101**, 2815 (1979).

[44] B.-K. Teo, M. R. Antonio, and B. A. Averill, *J. Am. Chem. Soc.* **105**, 3751 (1983).

for a particular absorber–scatterer pair involves using only data from structurally characterized (model) compounds. Two methods are available for doing this. The first involves parameterization of the functions and was pioneered by Hodgson and coworkers.[45] The particular parameterized amplitude and phase functions used are given by

$$B_s|f_s(\pi,\mathbf{k})| = c_0 \exp(-c_1\mathbf{k}^2)/\mathbf{k}^{c_2} \tag{42}$$

$$\alpha_{as}(\mathbf{k}) = a_0 + a_1\mathbf{k} + a_2\mathbf{k}^2 + a_{-1}\mathbf{k}^{-1} \tag{43}$$

[In the $\alpha_{as}(\mathbf{k})$ expression, usually *either* a_2 or a_{-1} are set to zero.] With this method, EXAFS data from a model compound are usually curve-fit with R_{as} and N_s for the shell fixed at the known values, and the c_i and a_i parameters are optimized. These parameter values are then fixed for use of the amplitude and phase functions in optimizations on data from a compound of unknown structure.

An alternate method for extracting amplitude and phase functions from model compounds involves the Fourier filtering and complex back-transform techniques already discussed. Equations (40) and (41) indicate that knowledge of R_{as} (for the model compound) allows calculation of $\alpha_{as}(\mathbf{k})$ from $\Phi(\mathbf{k})$ (generated in the complex backtransform) and knowledge of R_{as}, N_s, and σ_{as} allows calculation of $B_s|f_s(\pi,\mathbf{k})|$ from $A(\mathbf{k})$. Thus, except for the fact that σ_{as} is not available generally, one need make no assumptions about the functional form of the amplitude and phase functions [as required by Eqs. (42) and (43)] to calculate them as discrete functions empirically.

One of the main problems with any of the curve-fitting approaches described is the general lack of knowledge concerning the Debye–Waller σ_{as} for any particular compound. As already discussed, this term describes both static and dynamic variations in R_{as} within a particular shell. A crystallographic structural determination allows calculation of the static contribution [by Eq. (3)], but the dynamic contribution (due to thermal vibrations of the a–s bond) is only accessible for very symmetric compounds through use of vibrational frequencies and a normal coordinate analysis.[46] Curve-fitting analysis of EXAFS data on simple compounds can yield in principle σ_{as} values (by optimization of R_{as}, N_s, and σ_{as}) but the values of N_s and σ_{as} are highly correlated causing such a determination to be very error prone. These problems with σ_{as} have con-

[45] S. P. Cramer, K. O. Hodgson, E. I. Stiefel, and W. E. Newton, *J. Am. Chem. Soc.* **100**, 2748 (1978).

[46] S. J. Cyvin, "Molecular Vibrations and Mean Square Amplitudes." Elsevier, Amsterdam, 1968.

tributed significantly to the inability of practitioners of EXAFS to predict coordination numbers with accuracy any better than $\sim \pm 25\%$.

Described below is a hybrid method of curve-fitting analysis used with some success in the author's laboratory which attempts to use the strengths of both the theoretical and empirical approaches to circumvent some of the problems mentioned above. This method has some characteristics in common with the FABM method[44] but differs principally in that empirically derived amplitude and phase functions are used for the ultimate curve-fitting.

In outline, the method consists of (1) establishing a k-scale for both model and unknown data (by E_0 adjustment) which is compatible with the theoretical functions for the particular a–s pair; (2) assuming that the overall shape of the theoretical amplitude function is correct and using this to estimate a Debye–Waller factor for the model data; (3) using the known structural parameters and the estimated Debye–Waller factor for the model to extract (by complex backtransform) empirical amplitude and phase functions derived from the model; and (4) using these functions to perform curve-fitting on unknown data.

An example will serve to illustrate the method. The EXAFS data displayed in Fig. 11a are from a [4Fe–4S] cluster analog of Fe–S protein active sites. As an example, the Fe–S shell of this model compound will be used to generate amplitude and phase functions for curve-fitting. These functions should then be useful in fitting Fe–S shells in data from compounds of unknown structure. The first step is to Fourier filter just the Fe–S contribution as illustrated in Fig. 12c and d. This complex backtransform also generates the $\Phi(k)$ function (Fig. 13b) for this shell [by Eq. (38)]. Using the known average Fe–S distance from crystallographic data ($R_{as} = 2.280$ Å[47]), an empirical phase function [$\alpha_{as}(k)$] may be extracted from $\Phi(k)$ using Eq. (41). The $\alpha_{as}(k)$ calculated will depend upon the value of E_0 chosen to define the k-scale of the original EXAFS data (and to a lesser extent on the reverse FT window limits) and the empirical $\alpha_{as}(k)$ functions for three different choices of E_0 are plotted in Fig. 14. Also plotted in Fig. 14 is the theoretical phase function for Fe–S as calculated by Teo and Lee.[43] In order to place the empirically derived amplitude and phase functions to be used in this method on the same k-scale as the theoretical functions, E_0 is chosen as the value that yields empirical and theoretical phase functions that match as closely as possible. Figure 14

[47] The structural dimensions of the [4Fe-4S] core of [Fe$_4$S$_4$-(t-BuS)$_4$]$^{2-}$ were assumed to be the same as those for [Fe$_4$S$_4$(SC$_6$H$_5$)$_4$]$^{2-}$, taken from J. M. Berg and R. H. Holm, *in* "Iron-Sulfur Proteins" (T. G. Spiro, ed.), Metal Ions in Biology, Vol. 4, Chapter 1. Wiley, New York, 1982.
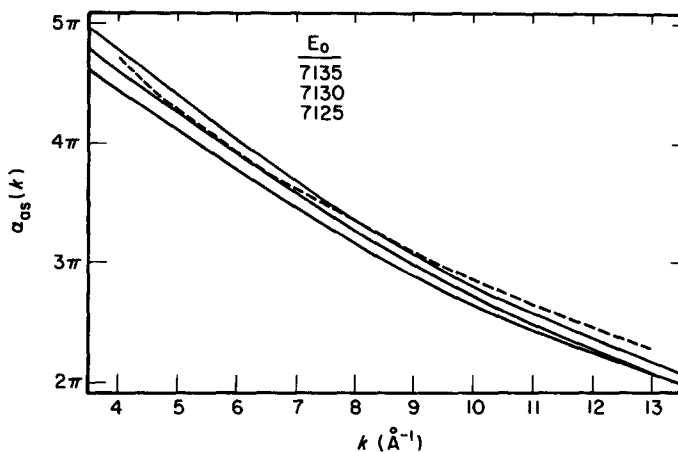
FIG. 14. Comparison of empirical and theoretical phase functions $[\alpha_{as}(k)]$. The empirical phase functions (solid lines) were extracted from the $\Phi(k)$ data of Fig. 13b as described in the text, with the original $\chi(k)$ data (Fig. 11a) extracted using different E_0 values (as indicated). The theoretical phase function is interpolated (using a third order polynomial) from values calculated by Teo and Lee in Ref. 43. This type of comparison is used to estimate the E_0 (7135 eV for this example) which places the observed data on the same k-scale as that used in generation of the theoretical functions.

suggests that $E_0 = 7135$ eV is a reasonable value for the Fe–S interaction in this example.

Once the k-scale is defined, the next step involves estimation of the Debye–Waller σ_{as} value for the model data. This consists of curve-fitting the model data using the empirical phase function determined above and the theoretical amplitude function given by Teo and Lee.[43] R_{as} and N_s are fixed at the known values and B_s and σ_{as} are optimized (while ΔE_0 is fixed at 0). For our example, this curve-fitting gives optimized values of $B_s = 0.354$ and $\sigma_{as} = 0.053$ Å. With the assumption that the shape (but not necessarily the absolute magnitude) of the theoretical amplitude function is correct, we can use this optimized value of σ_{as} as a physically meaningful one. Even if the assumption is invalid, this Debye–Waller σ_{as} can be used for comparison in fits of data from compounds of unknown structure.

The next step consists of using this optimized σ_{as} along with the known R_{as} and N_s to extract an empirical amplitude function $[B_s|f_s(\pi,k)|]$ from $A(k)$ using Eq. (40). [$A(k)$ was calculated in the complex backtransform of Fig. 12c and d using Eq. (37).] With this, both empirical phase and empirical amplitude functions have been extracted from the model data
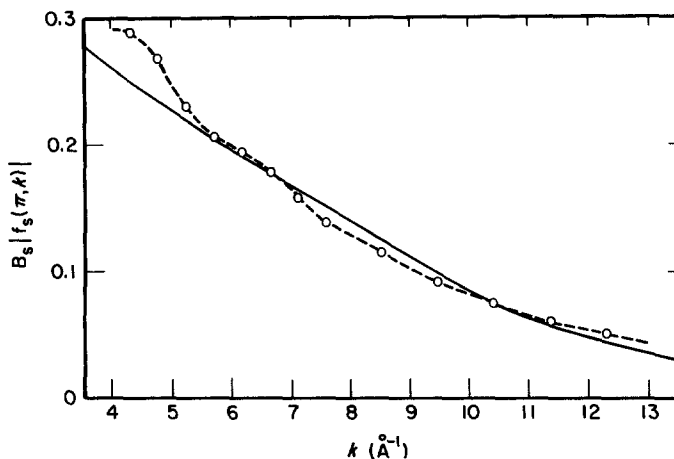
FIG. 15. Comparison of empirical and theoretical amplitude functions $[B_s|f_s(\pi, \mathbf{k})|]$. The empirical amplitude function (solid line) was extracted from the $A(\mathbf{k})$ data of Fig. 13a as described in the text. The theoretical amplitude function (O) consists of $|f_s (\pi, \mathbf{k})|$ values tabulated by Teo and Lee in Ref. 43 and $B_s = 0.354$ (see text). The points (O) indicate the tabulated values and the dashed line is calculated by interpolating between the points using a third-order polynomial.

and are now available for use in other curve-fitting. Figure 15 shows the extracted empirical amplitude function from the example and compares this function with the theoretical amplitude function as calculated by Teo and Lee.[43] [The theoretical amplitude function constitutes $|f_s(\pi, \mathbf{k})|$ and this is multiplied by the best fit scale factor, $B_s = 0.354$, for display in Fig. 15.]

In using these empirical amplitude and phase functions for curve-fitting single shells of data from a compound of unknown structure one has the option of varying R_{as}, N_s, and σ_{as}. (For multishell fits, ΔE_0 may require adjustment for some of the shells.) One problem often encountered is the high degree of correlation of N_s and σ_{as}. One method of circumventing this problem involves allowing N_s to take on only integer values. (For example, separate optimizations may be performed fixing N_s at a different integer value for each one.) One may then use the optimized value of σ_{as} (along with the "goodness-of-fit" indicator from the least-squares optimization) to determine which fit is best. In order to judge reasonably the values of σ_{as} one must be able to assess how physically reasonable a σ_{as} is. The utility of the value calculated for σ_{as} in the model compound is thus to have a basis for judging σ_{as} values obtained in various fits on compounds of unknown structure.

Accuracy of Results

Whatever specific method is used for EXAFS data analysis, there are inherent limitations to the accuracy of the results obtained. These can be summarized best as error limits for the determination of the three quantities of interest: R_{as}, N_s, and Z (atomic number). The error in R_{as} is dependent upon the ability to measure the frequency of the EXAFS oscillations and also slightly dependent upon the proper choice of E_0. With any of the curve-fitting techniques described, a lower bound on this error is probably $\sim \pm 0.02$ Å.

Errors in predicted N_s values come from various sources. First, distortions in the EXAFS amplitudes resulting from improper data collection (e.g., the thickness effect) will result in a systematic underestimation of N_s. For spectroscopically dilute samples, noise in the EXAFS data can combine with spurious beam artifacts (e.g., glitches) to cause random errors in N_s determination. (This is less of a problem in R_{as} determinations.) Probably most important is the contribution of the Debye–Waller factor to the overall EXAFS amplitude. Since independent knowledge of the proper value of σ_{as} is very difficult to come by, misestimation of this factor contributes to large errors in N_s. In the past, these factors have all contributed to errors in calculated N_s values as large as $\pm 30\%$. Although adequate testing has not yet been performed, it is hoped that the hybrid method of data analysis described above will be able to improve this error.

The atomic number, Z, of the scattering atom(s) is determined indirectly by finding which phase and amplitude functions fit the data best. Therefore, the error in Z is dependent on our ability to distinguish among phase and amplitude functions for adjacent elements in the periodic table. A typical error limit on Z is assumed to be $\Delta Z \approx \pm 1$. This means, for example, that C, N, and O are difficult to distinguish since their phase and amplitude functions all look fairly similar. This error limit applies to relatively low-Z scatterers. For metal scatterers, it should be increased probably to $\Delta Z \approx \pm 2$.

Conclusion

This chapter was written with one purpose in mind: broader exposure of the scientific community to the methodological details of the EXAFS technique will allow more critical examination of published data and eventually result in higher quality work and more acceptance of EXAFS as a useful structural technique. As with any infant technique, expectations have run the gamut: EXAFS is not the savior of bioinorganic and

biophysical chemists, but it does have a niche to fill. Any potential (or current) EXAFS practitioners must be aware of both the strengths *and* the limitations of the technique. It is hoped that this chapter has made some small contribution toward a more rational use of the EXAFS technique in the study of biological systems.

[24] Velocity Sedimentation Study of Ligand-Induced Protein Self-Association

By GEORGE C. NA and SERGE N. TIMASHEFF

A large number of protein reactions are regulated through the reversible stoichiometric interactions with small molecules or ligands. Within this wide spectrum of protein reactions, the reversible association and dissociation of protein subunits have drawn considerable research interest. The biological significance of such interactions is evident. Subunit associations are ubiquitous in key enzymes regulating metabolic pathways, in the formation of cellular organelles, and in regulatory and transporting proteins.

This chapter is devoted to the methodology of studying ligand-induced protein self-associations using the velocity sedimentation technique. The type of study described here is aimed at characterizing macromolecular associations in terms of their stoichiometries and equilibrium constants, as well as at elucidating ligand bindings to macromolecules and the equilibrium linkages between the ligand binding and the self-association reactions. The discussion is restricted to fast and reversible self-association systems. Special emphasis is given to the experimental considerations and the methods of data analysis. Theoretical treatments are minimized and limited to providing a basic conceptual framework for the data analysis. There have been several excellent articles in previous volumes of this series and elsewhere dealing with similar subjects.[1-3] The readers should consult them for references.

This chapter is divided into four sections. The first section consists of a general consideration of the experimental approach in the velocity sedimentation of ligand-induced self-association system. The second section

[1] L. M. Gilbert and G. A. Gilbert, this series, Vol. 48, p. 195.
[2] J. R. Cann, this series, Vol. 48, p. 299.
[3] D. J. Winzor, *in* "Protein-Protein Interactions" (C. Frieden and L. W. Nichol, eds.), p. 129. Wiley, New York, 1981.